1989

Preparation and processing of ZnS powders with spherical submicron particles

Ahmet Celikkaya
Iowa State University

Order Number 9003506

Preparation and processing of ZnS powders with spherical submicron particles

Celikkaya, Ahmet, Ph.D.

Iowa State University, 1989

U·M·I
300 N. Zeeb Rd.
Ann Arbor, MI 48106

Preparation and processing of ZnS powders with spherical submicron particles

by

Ahmet Celikkaya

A Dissertation Submitted to the
Graduate Faculty in Partial Fulfillment of the
Requirements for the Degree of
DOCTOR OF PHILOSOPHY

Department: Materials Science and Engineering
Major: Ceramic Engineering

Approved:

Signature was redacted for privacy.

In Charge of Major Work

Signature was redacted for privacy.

For the Major Department

Signature was redacted for privacy.

For the Graduate College

Iowa State University
Ames, Iowa

1989

TABLE OF CONTENTS

	Page
GENERAL INTRODUCTION	1
Objectives	5
Explanation of Dissertation Format	5
SECTION I. PREPARATION AND MECHANISM OF FORMATION OF SPHERICAL SUBMICRON ZnS POWDERS	7
ABSTRACT	8
INTRODUCTION	9
EXPERIMENTAL	11
Materials	11
Precipitation	11
Characterization	12
RESULTS AND DISCUSSION	13
Determination of Critical Supersaturation	13
Effect of Sulfide Ion Generation Rate on Particle Size Distribution	18
Mechanism of Particle Formation and Growth	26
CONCLUSIONS	40
REFERENCES CITED	41
ACKNOWLEDGMENTS	42
SECTION II. MORPHOLOGY OF ZnS PARTICLES PRODUCED FROM VARIOUS ZINC SALTS BY HONOGENEOUS PRECIPITATION	43
ABSTRACT	44
INTRODUCTION	45

Page

EXPERIMENTAL 49

Precipitation 49

Characterization 50

RESULTS AND DISCUSSION 51

Effects of Supporting Anion on Precipitation Kinetics 51

Effect of Supporting Anion on Particle Morphology 56

Nitrate system 56
Sulfate system 58
Chloride system 65
Acetate system 70

CONCLUSIONS 73

REFERENCES CITED 74

ACKNOWLEDGMENTS 75

SECTION III. HOT PRESSING OF ZnS POWDERS WITH SUBMICRON PARTICLES 76

NOMENCLATURE 77

ABSTRACT 78

INTRODUCTION 79

EXPERIMENTAL 86

RESULTS AND DISCUSSION 88

Green Compact 88

Densification 91

Microstructure Evolution 99

Densification Mechanisms 111

CONCLUSIONS 129

	Page
REFERENCES CITED	130
ACKNOWLEDGMENTS	132
GENERAL CONCLUSIONS	133
LITERATURE CITED	135
ACKNOWLEDGMENTS	136

GENERAL INTRODUCTION

Infrared-transmitting ceramics find use in various applications, including infrared lenses and related components, windows, and domes that function primarily to protect detecting devices from the environment. Such applications necessitate bulk infrared materials. Although requirements for infrared-transmitting materials are set by the particular application, the most demanding applications require ceramics that are strong, tough and have high thermal shock resistance. A variety of strong oxide ceramics are infrared transparent in the 3-5 μm range. However, only a few materials have an "acceptable" combination of thermomechanical properties and useful transparency in the 8-12 μm region. This dilemma arises because the same factors that contribute to long wavelength (8-12 μm) transparency, i.e., weak chemical bonding between heavy atoms, give rise to low mechanical strength.

Most optical ceramics are melted and formed into shapes by glass making techniques. They are useful in this form as their amorphous structure and absence of grain boundaries permit the passage of radiation over a wide spectrum only with reflections from surfaces, minimum scattering from retained bubbles, and low absorption due to purity. However, there are a growing number of applications that cannot be successfully satisfied by available glasses. Crystalline optical components with superb chemical and physical properties can also be produced by melt techniques, but in this case, one must seed

and grow single crystals to result in useful materials for optical applications. These components tend to be small, expensive and hard to grow into useful shapes. In addition, due to the brittleness of most ceramics, single crystalline components are not desired for critical applications. Polycrystalline ceramics can fulfill the applications not satisfied by glass or single crystalline materials. However, an optimum combination of optical and mechanical properties can be achieved only by fully-dense, fine-grained and uniform microstructures. The development of processing methods that reproducibly produce ceramic components with this kind of microstructures constitutes much of the research in the field of ceramic processing. A promising approach for achieving this goal may be to begin with powders with submicron, monosized and monodispersed particles in order to produce a uniform starting microstructure.

This study involved the preparation and processing of spherical, submicron ZnS powders for infrared applications. Thermomechanical properties of ZnS form the baseline against which other strong, high temperature, long wave infrared-transmitting materials must be compared. For this reason, it is important to improve the mechanical properties of ZnS, thereby allowing more demanding applications of ZnS. Table 1 gives a summary of physical properties of some existing infrared (8-12 μm) optical ceramic materials [1]. The properties of ZnS listed in Table 1 belong to a commercially available, hot-pressed material with grain sizes ranging between 5-10 μm. There is evidence that reducing grain size to submicron level and/or imbedding micro-sized

Table 1. Summary of properties of some existing long wave (8-12 μm) infrared-transmitting materials

	ZnS	GaAs	GaP	Si	Ge	Diamond
Density ($g \cdot cm^{-3}$; 23°C)	4.08	5.32	4.13	2.33	5.32	3.52
Hardness ($kg \cdot mm^{-2}$; 23°C)	230	700	845	1150	850	9000[a]
Flextural strength (psi; 23°C)	14000	8000	15000	18500	13500	427000
Young's modulus (GPa; 23°C)	74.50	85.50[b]	102.60[b]	130.10[b]	130.30[b]	1050
Poisson's ratio	0.29	0.31	0.31	0.28	0.28	0.16
Thermal expansion ($10^{-6} \cdot K^{-1}$; 23°C/200°C)	6.80/7.70	5.73/6.36	5.30/5.80	2.30/2.90	6.00	1.00/2.00
Thermal conductivity ($W \cdot cm^{-1} \cdot °K^{-1}$; 23°C)	0.17	0.53	0.97	1.41	0.60	26.00

Fracture toughness ($MPa \cdot m^{1/2}$; 23°C)	1.00	0.43[b]	0.80[b]	0.95[b]	0.66[c]	26.00[d]
Melting temperature (°C)	1830	1238	1467	1420	937	--
Band gap (eV; 23°C)	3.58[e]	1.43[e]	2.24[f]	1.12[f]	0.67[f]	5.40[f]
Crystal structure	ZnS	ZnS	ZnS	Diamond	Diamond	Diamond

[a]Data taken in the 111 plane.

[b]Data taken in the 100 plane.

[c]Data estimated from rapture modulus.

[d]Estimate.

[e]Direct transition.

[f]Indirect transition.

whiskers in a matrix of submicron grain size will enhance mechanical behavior [2, 3]. In other cases, there is a need for ZnS powders with uniform, submicron particles with known densification behavior.

Objectives

The primary objectives of this research were to prepare high purity ZnS powders with spherical submicron particles, to access the influence of various experimental parameters on powder characteristics, and to understand the kinetics of particle formation. Another objective of the research was to process these powders into dense ceramic parts, and to elucidate mechanism(s) of densification under various processing conditions.

Explanation of Dissertation Format

This dissertation is arranged in accordance to the alternate dissertation format described in the Graduate College Thesis Manual, and consists of three separate manuscripts prepared for publication. The first paper, "Preparation and Mechanism of Formation of Spherical Submicron ZnS Powders", has been submitted to the Journal of Colloid and Interface Science. The second and third papers, "Morphology of ZnS Particles Produced from Various Zinc Salts by Homogeneous Precipitation" and "Hot Pressing of ZnS Powders with Submicron Particles," will be submitted to the American Ceramic Society, and should be in print in 1989.

Note that although all three manuscripts are largely the work of this author, Dr. Mufit Akinc (major professor) has made significant contributions throughout the study and appears as co-author on these papers.

SECTION I. PREPARATION AND MECHANISM OF FORMATION OF SPHERICAL SUBMICRON ZnS POWDERS

ABSTRACT

Spherical, submicron particles of zinc sulfide were homogeneously precipitated by thermal decomposition of thioacetamide in acidic aqueous solutions. The rate of sulfide ion generation, determined by various combinations of temperature, pH, and initial concentrations of zinc ions and of thioacetamide, as related to particle growth rate had the paramount effect on the particle size distribution. Monosized, bimodal or narrow size distribution powders were obtained under certain combinations of experimental variables. Particles were found to be porous agglomerates of ~15 nm sphalerite crystallites. Particle growth was determined to proceed through diffusion-controlled aggregation of crystallites.

INTRODUCTION

Zinc sulfide is an attractive infrared window material as it possesses good IR transmittance in the 8-12 μm range as well as high melting temperature. When a polycrystalline material is used for applications such as this, a uniform final microstructure is needed. Although starting powders consisting of spherical, submicron particles are normally considered desirable, there is no general agreement as to whether particle assemblies with a narrow or a wide size distribution are more preferable for achieving a theoretically dense uniform microstructure. It is well known that random packing of particles with a size distribution yields denser green compacts than do monosize particles. On the other hand, monosize powder assemblies are believed to sinter more uniformly and so result in a more uniform sintered microstructure. Ability to control precipitation variables in order to yield reproducible ceramic powders with spherical, submicron particles having a specific type of particle size distribution in sufficient quantities is a prerequisite to the understanding of variables that influence packing efficiency and uniformity of initial and final microstructure.

Zinc sulfide has long been prepared by a variety of methods, including gas phase, solid/vapor and aqueous solution reactions [1-5]. Chiu [3] was the first to prepare monosized, spherical particles of sulfides of several metals, including zinc. His procedure involved complexing zinc ions with EDTA, followed by precipitation by bubbling

H_2S gas through the solution. A mean particle diameter of 0.2 μm was obtained employing very low zinc ion concentrations ($<10^{-3}$M). Later, Wilhelmy and Matijevic [4] employed thermal decomposition of thioacetamide (TAA) to prepare micron-sized spherical particles by aging the reaction mixture several hours using a two-step procedure. Williams et al. [5] employed the same technique to prepare monosized, spherical particles of ZnS about 3 μm in diameter. In this case, however, the critical nuclei appeared as faceted single crystals rather than the spherical, submicron "seeds" observed by Wilhelmy and Matijevic [4], and the resulting powder was a mixture of sphalerite (cubic) and wurtzite (hexagonal) phases.

The main objective of this work was to investigate the influence of experimental variables on the morphology of the ZnS particles produced by thioacetamide decomposition and to understand the mechanism of particle formation.

EXPERIMENTAL

Materials

Reagent grade TAA (99% pure) was supplied by Aldrich Chemical Company. All other chemicals used in this study were Fisher reagent grade and were used without further purification.

Precipitation

A stock solution of zinc ions was prepared by dissolving $Zn(NO_3)_2 \cdot 6H_2O$ in deionized water and then filtering through 0.1 μm cellulose nitrate membrane filters to give a final zinc ion concentration of 1.56 M. An 8.3 mL aliquot of this stock was transferred into a beaker and nitric acid solution (0.1 N or 0.01 N) was added to bring the total volume slightly less than 250 mL. The solution was heated to reaction temperature, the desired amount of thioacetamide was added and final volume was brought to 250 mL. The beaker was then immersed in a water bath at the set reaction temperature. After a certain period of aging, a bluish tint in the solution was judged to indicate the onset of precipitation. The time interval necessary to induce the change in the solution color was recorded. Thirty milliliter aliquots were collected and quenched to 15°C periodically after precipitation had started. A number of combinations of experimental variables were investigated. Aging temperatures of 60, 70 and 80°C were employed. Initial thioacetamide concentrations were varied to give $[TAA]_0/[Zn]_0$ ratios of 4, 8 and

16 for pH = 1 and pH = 2. The initial zinc ion concentration $[Zn]_o$ was held constant at 0.05 M in all experiments.

Characterization

The change of particle size distribution over time was determined by a centrifugal particle size analyzer using a portion of 30 mL aliquots collected at various times during the aging process. The remainder of the aliquot was centrifuged at 5000 rpm for 30 minutes and the recovered precipitate was washed once with deionized water and once with acetone. A drop of suspension in acetone was placed on an aluminum foil and dried for observation of morphology by SEM. Selected area electron diffraction patterns were obtained to determine structure of individual particles. X-ray diffraction spectra of the powders were also obtained to determine crystallite sizes and phase purity of the powders. Specific surface areas of the powders were determined by a single point BET method using a N_2-He gas mixture.

RESULTS AND DISCUSSION

Determination of Critical Supersaturation

Homogeneous precipitation of zinc sulfide by thermal decomposition of thioacetamide in acidic (pH < 3) aqueous solutions proceeds as follows:

$$CH_3C(S)NH_2 \xrightarrow{H_3O^+} CH_3C(O)NH_2 + H_2S \qquad (1)$$

$$H_2S \rightleftarrows HS^- + H_3O^+ \qquad K_1 = [HS^-][H_3O^+]/[H_2S] \qquad (2)$$

$$HS^- \rightleftarrows S^= + H_3O^+ \qquad K_2 = [S^=][H_3O^+]/[HS^-] \quad . \qquad (3)$$

Swift and Butler [6] had studied the kinetics of TAA decomposition, the rate determining step, and found a rate expression of

$$-\frac{d[TAA]}{dt} = k[H_3O^+][TAA] \quad . \qquad (4)$$

For the rate constant, k, an Arrhenius type expression was found with a pre-exponential factor of 6.58×10^{11} $L.mole^{-1}.min^{-1}$ and an activation energy of 79.87 $kJ.mole^{-1}$. The total concentration of sulfide species at time t can then be found by recognizing that $[TAA]_o - [TAA]_t = [S]_{total} = [H_2S] + [HS^-] + [S^=]$ and integrating Eq. (4) from t = 0 to t = t to give:

$$[TAA]_o\ (1 - \exp(-k[H_3O^+]t)) = [H_2S] + [HS^-] + [S^=] \quad . \qquad (5)$$

Combining Eq. (5) with Eqs. (2) and (3) yields:

$$[TAA]_o\ (1 - \exp(-k[H_3O^+]t)) = \frac{[H_3O^+]^2[S^=]}{K_1K_2}$$

$$+ \frac{[H_3O^+][S^=]}{K_2} + [S^=] \qquad (6)$$

or, equivalently stated:

$$[S^=] = \frac{[TAA]_o\ (1-\exp(-k[H_3O^+]t))}{[H_3O^+]^2/K_1K_2 + [H_3O^+]/K_2 + 1} \quad . \qquad (7)$$

Accurate thermodynamic data are available in the literature for the dissociation reactions of H_2S and the formation of aqueous sulfide species at room temperature [7]. Assuming that $\Delta H°$ and $\Delta S°$ are constant over the temperature range studied, values of K_1, K_2, and solubility product K_{sp} for zinc sulfide at any temperature can easily be calculated. Expressions for these constants were calculated to be:

$$K_{1,T} = 8.71 \times 10^{-4} \exp\ (-5404.80/RT) \qquad (8)$$

$$K_{2,T} = 5919.46 \exp\ (-24{,}195.56/RT) \qquad (9)$$

$$K_{sp,T} = 2.30 \times 10^{-10} \exp(-17{,}575.45/RT) \qquad (10)$$

where R is the gas constant in Joules per mole per degree Kelvin. Using this information, the relative supersaturation at any time (t), which is defined as

$$S = \left(\frac{[Zn^{2+}]_t [S^{=}]_t}{K_{sp}} \right)^{1/2} , \qquad (11)$$

can be calculated for any combination of T, pH, and initial concentrations of TAA and zinc ions. Figure 1 shows the variation of S with time for various combinations of experimental parameters, assuming that no precipitation occurs. Also indicated on these curves are the times at which precipitation started with corresponding values of critical supersaturation for that particular combination of experimental variables. The value of critical supersaturation for nucleation remained more or less constant, around 8.5 in each case. This value of critical supersaturation found is an order of magnitude less than what Williams et al. [5] reported. The difference arises mainly due to differences in the K_{sp} values used. Williams et al. [5] used a K_{sp} of 4.8×10^{-23} at 75°C, whereas we estimated a value of 2.13×10^{-21} at the same temperature for cubic ZnS. All other constants used were of the same magnitude. Another contribution to the observed difference may arise from a stronger interaction between Zn^{++} and the $SO_4^{=}$ ions in the solution which they have employed as a

Figure 1. Variation of relative supersaturation S with time for various combinations of experimental parameters with $[Zn]_o$ = 0.5 M and

a) pH = 1, T = 60°C, $[TAA]_o/[Zn]_o$ = 4,
b) pH = 1, T = 60°C, $[TAA]_o/[Zn]_o$ = 8,
c) pH = 1, T = 70°C, $[TAA]_o/[Zn]_o$ = 4,
d) pH = 2, T = 60°C, $[TAA]_o/[Zn]_o$ = 4.

Values of critical supersaturation are also indicated for each case

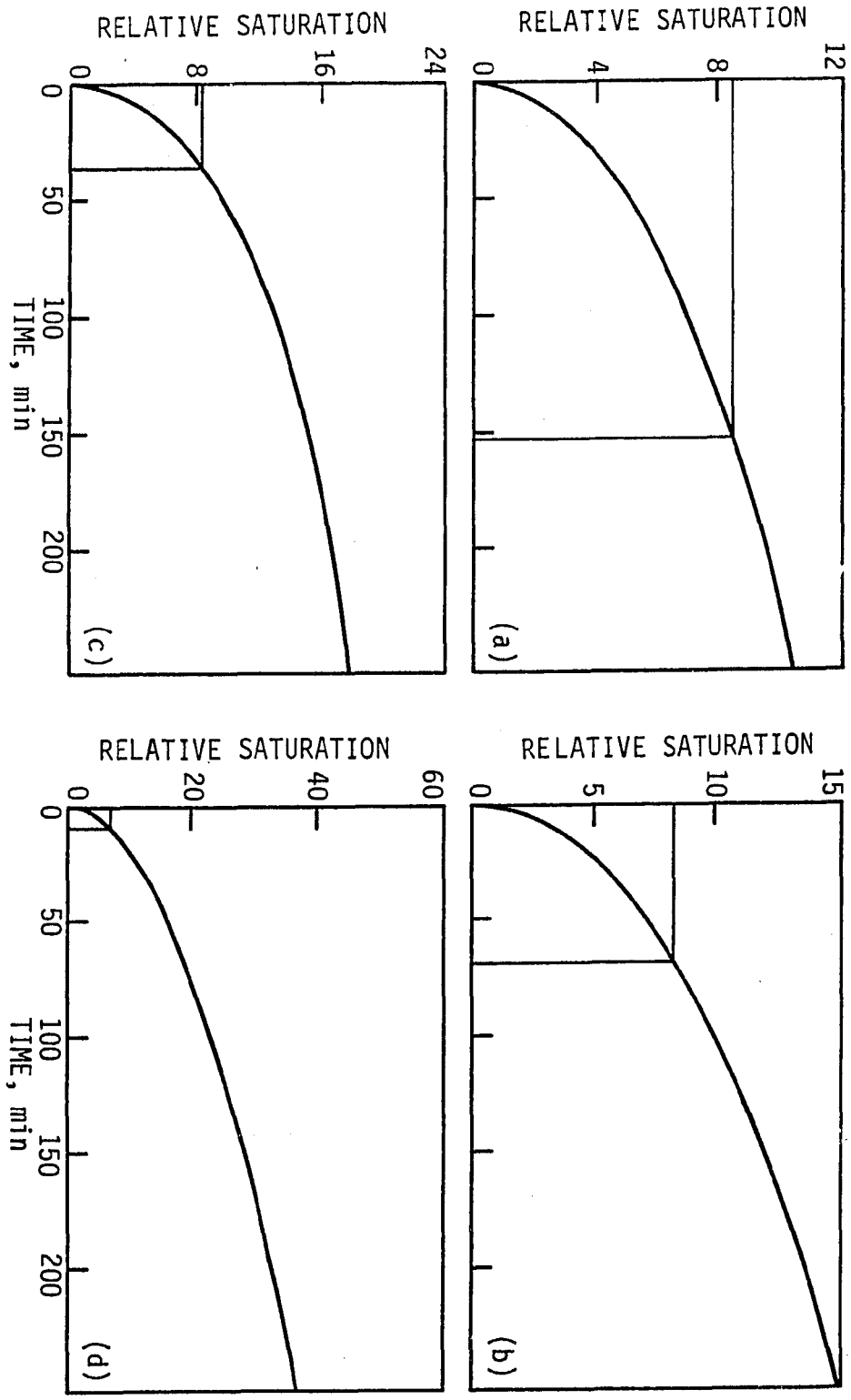
RELATIVE SATURATION
0
4
8
12
(a)
RELATIVE SATURATION
0
5
10
15
(b)
RELATIVE SATURATION
0
8
16
24
0
50
100
150
200
TIME, min
(c)
RELATIVE SATURATION
0
20
40
60
0
50
100
150
200
TIME, min
(d)

supporting anion as opposed to the NO_3^- in our study. Our experiments using sulfate salts showed a strong effect of $SO_4^=$ ions on the precipitation kinetics [8].

Effect of Sulfide Ion Generation Rate on Particle Size Distribution

Although the absolute value of relative supersaturation at the time of nucleation remained constant for various combinations of experimental parameters, the time needed to reach the critical relative supersaturation varied over two orders of magnitude. The reciprocal time to reach critical supersaturation is related to sulfide ion generation rate in the solution, and we have defined it as the 'rate-to-nucleation' for the context of this study. Table 1 gives the rate-to-nucleation for several combinations of experimental variables at $[Zn]_o$ = 0.05 M. The rate-to-nucleation had the paramount influence on the particle size distribution of the powders. Rates higher than 0.250 min^{-1} were the range where most variability in particle size distribution was observed.

Figure 2 shows an electron micrograph taken 180 min. after precipitation had started for run #2 (pH = 1, T = 60°C, $[Zn]_o$ = 0.05 M, and $[TAA]_o/[Zn]_o$ = 8) corresponding to a rate of 1.41 x 10^{-2} min^{-1}. Formation of the particles was first observed after 70 min. Growth of these particles with time is given in curve 'a' of Figure 3. The drop in the mean particle size for this run at 180 minutes is a result of formation of a second generation of particles, as may be

Table 1. Variation of rate of sulfide ion generation with various combinations of experimental parameters

Run #	Temperature (°C)	pH	$[TAA]_o/[Zn]_o$	Rate to nucleation (min^{-1})
1	60	1	4	6.6×10^{-3}
2	60	1	8	1.41×10^{-2}
3	70	1	4	2.70×10^{-2}
4	70	1	8	5.88×10^{-2}
5	70	1	16	1.11×10^{-2}
6	70	2	4	0.250
7	70	2	8	0.500
8	70	2	16	1.00
9	80	2	4	1.50
10	80	2	8	2.00
11	80	2	16	4.00

Figure 2. Scanning electron micrograph of particles obtained (with experimental parameters pH = 1, T = 60°C, $[Zn]_o$ = 0.5 M and $[TAA]_o/[Zn]_o$ = 8) 180 min. after precipitation started

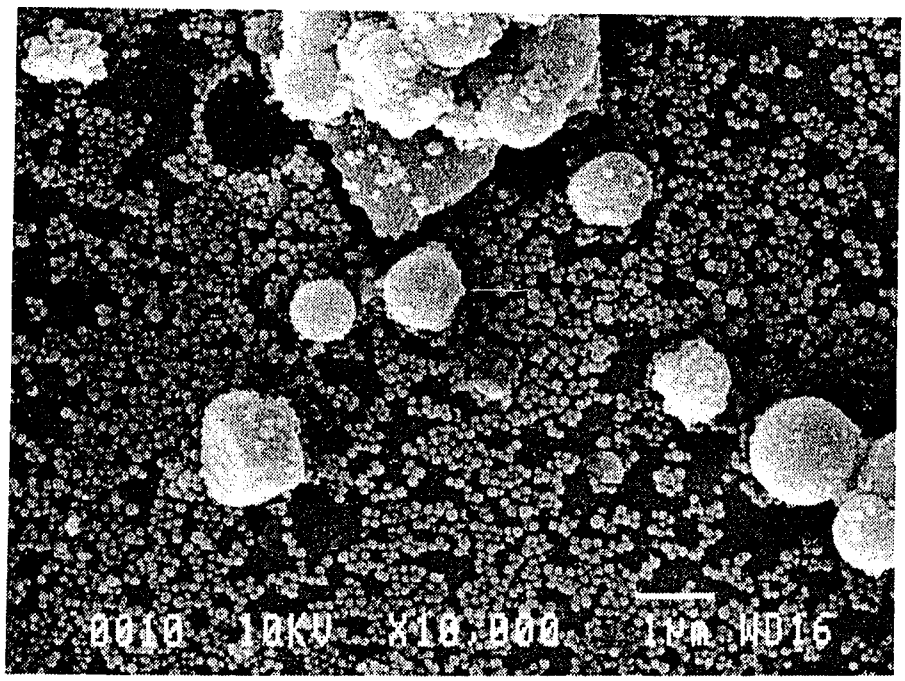
0010 10KV X10,000 1μm WD16

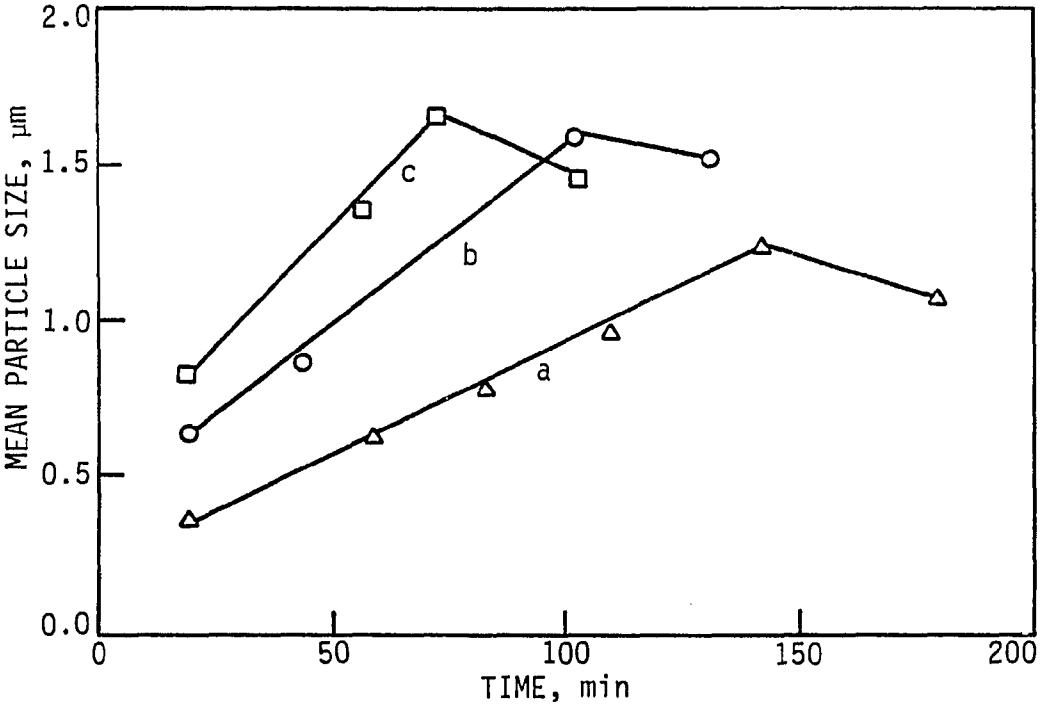

Figure 3. Variation of mean particle size with time for pH = 1, $[Zn]_o$ = 0.05 M and a) $[TAA]_o/[Zn]$ = 8, T = 60°C; b) $[TAA]_o/[Zn]$ = 4, T = 70°C; and c) $[TAA]_o/[Zn]_o$ = 8, T = 70°C

observed in the electron micrograph of Figure 2. Similar bimodal size distributions were observed for rate-to-nucleation values of up to 0.250 min^{-1}, with higher growth rates, as indicated by higher slopes of curves b and c in Figure 3, and shorter times for formation of second generation of particles, as demonstrated by the shift of maxima toward shorter times.

At least two plausible explanations can be offered for observing two generations of particles. First, as the initially formed particles reach a critical size (typically $\gtrsim$1 μm) where they can settle out of the solution, a new generation of particles may form from the solution. Secondly, if the rate of sulfide ion formation is slightly larger than the rate of its consumption in the growth process, a build-up of excess sulfide ions may result in formation of a second generation of particles. The first mechanism does not appear to be likely, as calculations based on the limiting size of first generation particles show that settling times are approximately the same as the total aging time.

At intermediate rates, such as 0.250 to 1.00 min^{-1}, the population density of first generation particles is high enough that growth of these particles can maintain $[S^{=}]$ low enough to prevent formation of second generation particles, and hence, monosize particles are obtained. Figure 4 shows micrographs of precipitates for run #7 at various precipitation times. The precipitation was completed (~100% recovery) in approximately one hour with a final mean particle size of about 0.5 μm.

Figure 4. Scanning electron micrographs of particles obtained with experimental parameters being pH = 2, T = 70°C, $[Zn]_o$ = 0.05 M and $[TAA]_o/[Zn]_o$ = 8 at

a) 5 mins. after precipitation started,
b) 10 mins. after precipitation started,
c) 15 mins. after precipitation started,
d) 40 mins. after precipitation started

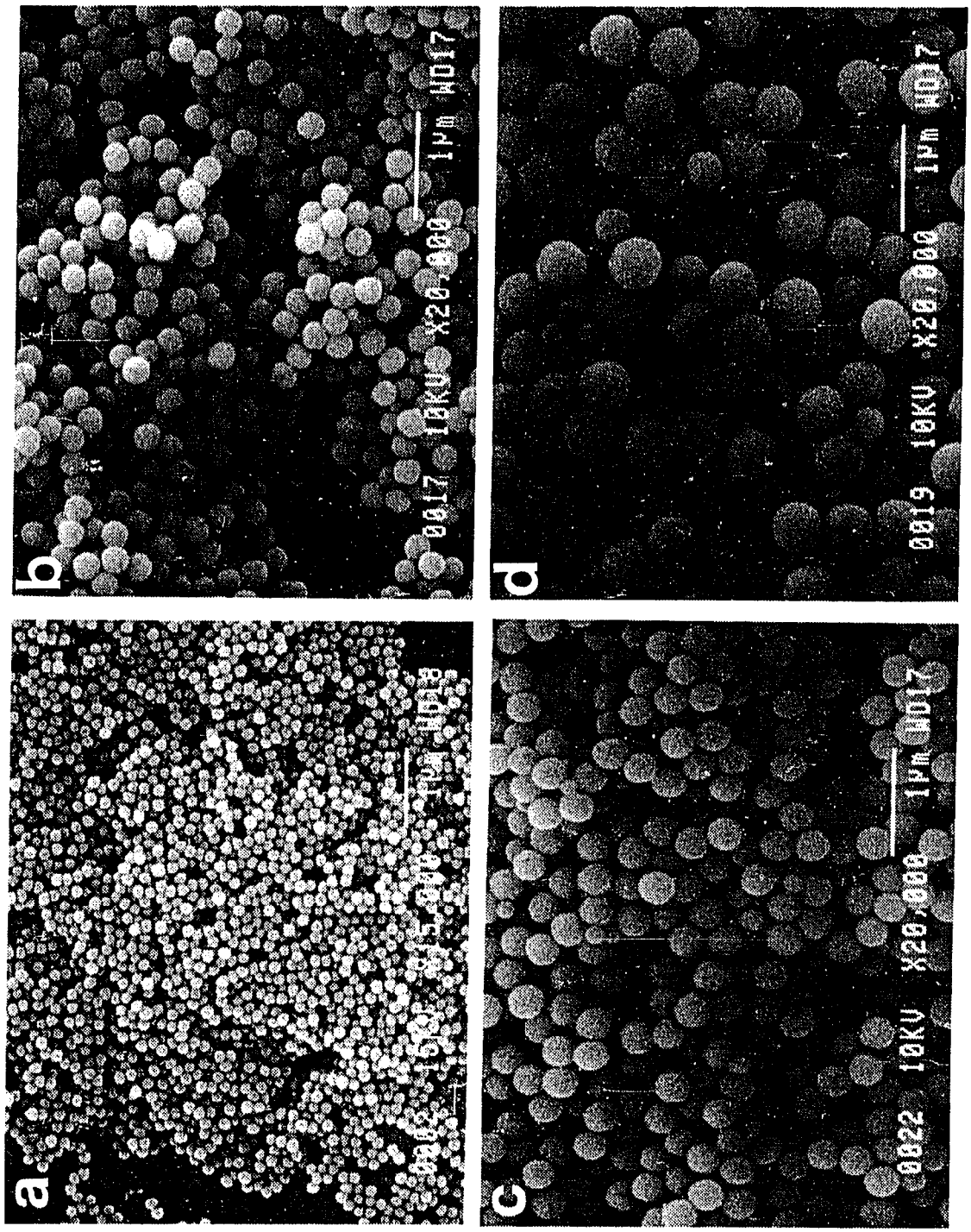
a
0002 15KV X5,000 1μm WD18
b
0017 10KV X20,000 1μm WD17
c
0022 10KV X20,000 1μm WD17
d
0019 10KV X20,000 1μm WD17

At still higher rate-to-nucleation (specifically at around 1.00 to 1.50 min^{-1}), a bimodal particle size distribution was again obtained, with larger particles (first generation) having a mean size of about 0.6 μm at the end of precipitation. A scanning electron micrograph of such a sample is given in Figure 5. Observation of bimodal size distribution at high rates supports the earlier paradigm that the second generation of particles is a direct consequence of growth rate not keeping up with the sulfide ion generation rate, resulting in a net sulfide ion build-up in the solution.

Beyond a rate of 1.50 min^{-1}, a continuous distribution of particle sizes was obtained, as shown by the electron micrograph of particles obtained for run #10 in Figure 6. As indicated in the figure, particle size ranges between 0.2 and 0.5 μm and distribution is continuous.

Mechanism of Particle Formation and Growth

Specific surface area values for a large number of samples were found to be around 50 m^2/g. This value of surface area is much higher than the value of 4.87 m^2/g expected for a monosize powder having a mean particle diameter of 0.3 μm, and corresponds to an equivalent spherical diameter of about 29 nm. The apparent discrepancy between the observed mean particle diameter and the equivalent spherical diameter, calculated from specific surface area value, can be resolved if one assumes that the large particles (~0.3 μm) are extremely

Figure 5. Scanning electron micrograph of ZnS particles obtained under the conditions pH = 2, T = 80°C, $[Zn]_o$ = 0.05 M and $[TAA]_o/[Zn]_o$ = 4

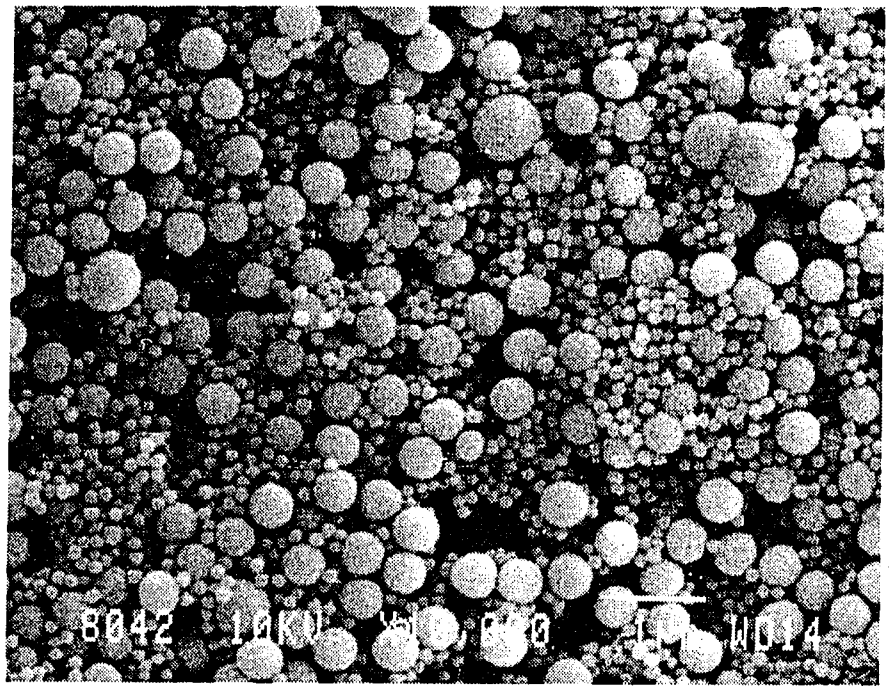
8042 10KV

Figure 6. Scanning electron micrographs of ZnS particles obtained when pH = 2, T = 80°C, $[Zn]_o$ = 0.05 M and $[TAA]_o/[Zn]_o$ = 8

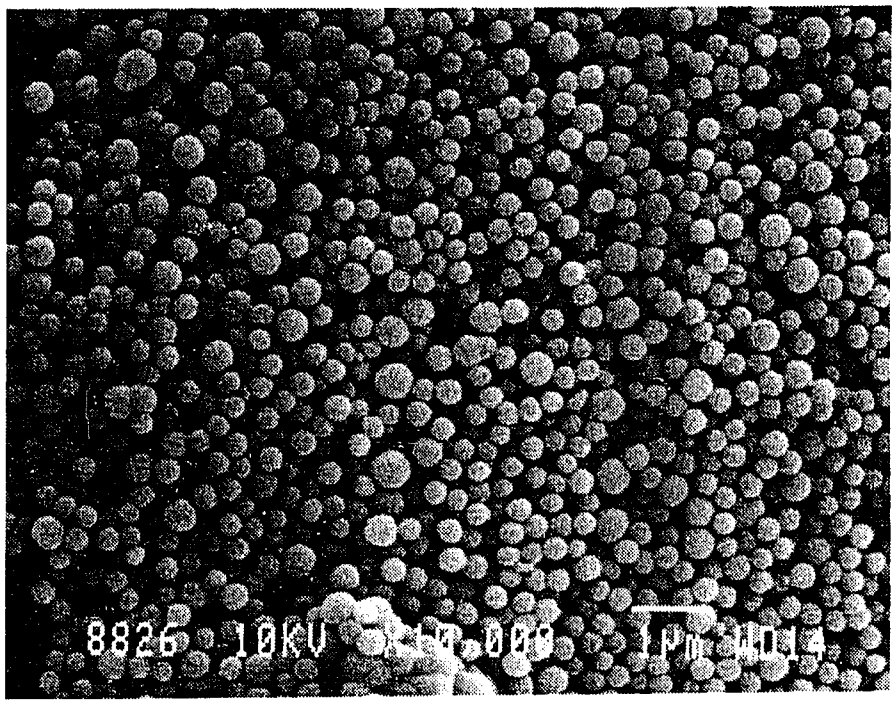
8826 10KV

porous or are collections of much smaller (~29 nm) crystallites.

A transmission electron micrograph and selected area diffraction pattern of a monosize powder are shown in Figure 7. As the figure clearly indicates, the spherical particles are actually agglomerates of about 14 nm crystallites which the diffraction pattern shows to be sphalerite. An independent determination of the crystallite size was made with the X-ray diffraction line broadening technique. The crystallite size was found to be 13 nm, in reasonably good agreement with the values obtained by surface area and TEM observations.

Alternatively, one can estimate the size of the nuclei that form during the precipitation using a modified form of the Kelvin equation [9]:

$$\frac{RT}{M} \ln \frac{a_r^*}{a} = \frac{2\gamma}{\rho r^*} \tag{12}$$

where

a_r^* = the activity of the ions in equilibrium with a nucleus having a critical radius r^*,

a = the activity of ions in equilibrium with a macroscopic crystal phase,

γ = the interfacial tension between solid and liquid phase,

ρ = the density of the solid,

M = the molecular weight,

R = the gas constant, and

Figure 7. Transmission electron micrograph of sample given in Figure 4(b) and selected area diffraction pattern of the particles

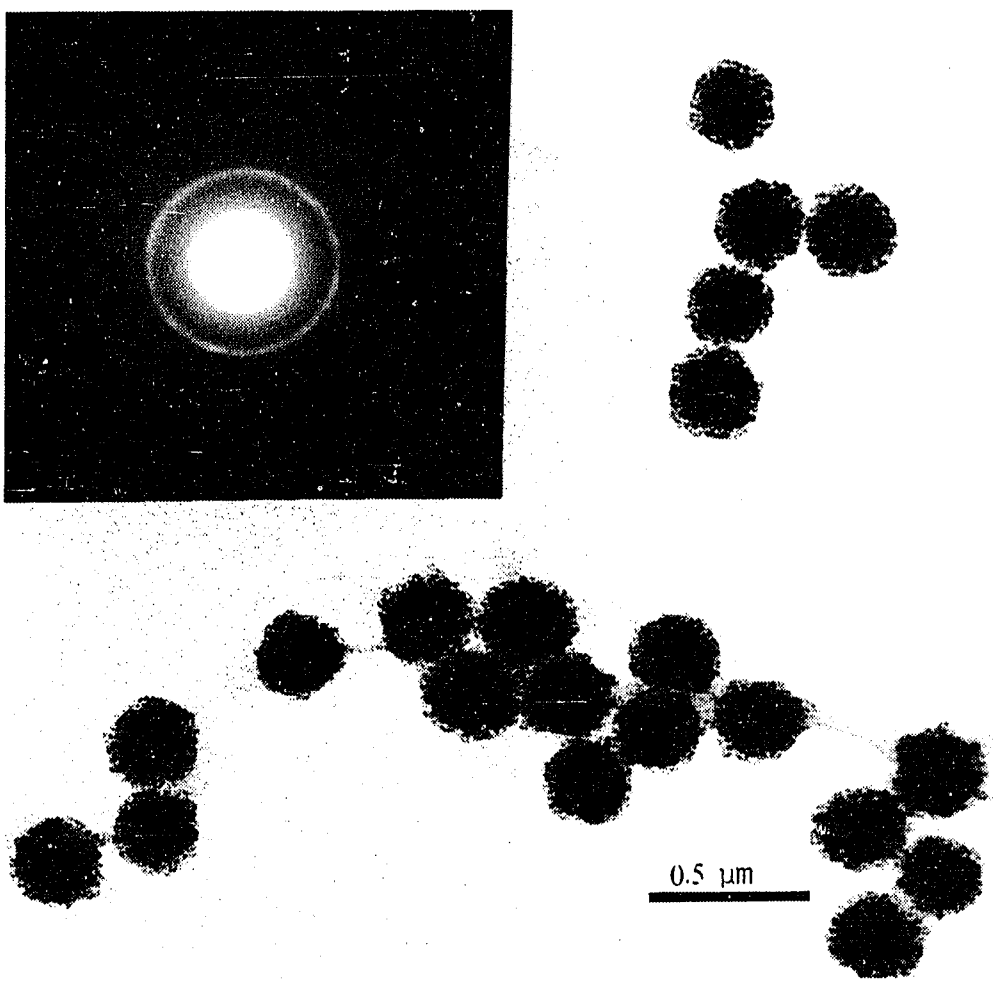
0.5 µm

T = absolute temperature.

Comparison of this equation with Eq. (11), and assuming that the activity coefficient is unity and that the ionic strengths of the solution in equilibrium and in supersaturated condition are roughly the same [10], gives:

$$2 \frac{RT}{M} \ln S = \frac{2\gamma}{\rho r^*} \quad . \tag{13}$$

Using this equation and substituting 1.672 J/m^2 for γ (for the {100} face of sphalerite) and a density of 4.10 Mg/m^3, the critical nucleus size at a relative supersaturation of 8.5 is found to be 13 nm, which is in excellent agreement with the crystallite sizes determined experimentally. This implies that the nuclei, once formed, do not grow significantly and growth of spherical particles occurs through agglomeration of 13 nm size sphalerite crystallites. The agglomeration time necessary to reduce the population of these crystallites by half is estimated to be less than one second assuming no barrier for agglomeration. Since the precipitation was carried at low pH near its isoelectric point [4], agglomeration is likely to proceed quite rapidly preventing growth of individual nuclei.

A straight line was obtained when the diffusion chronomal, I_D, was plotted against time (Figure 8) for particle growth of monosized powders for run #7, indicating that the growth was a diffusion controlled process [11]. The diffusion coefficient, D, is proportional

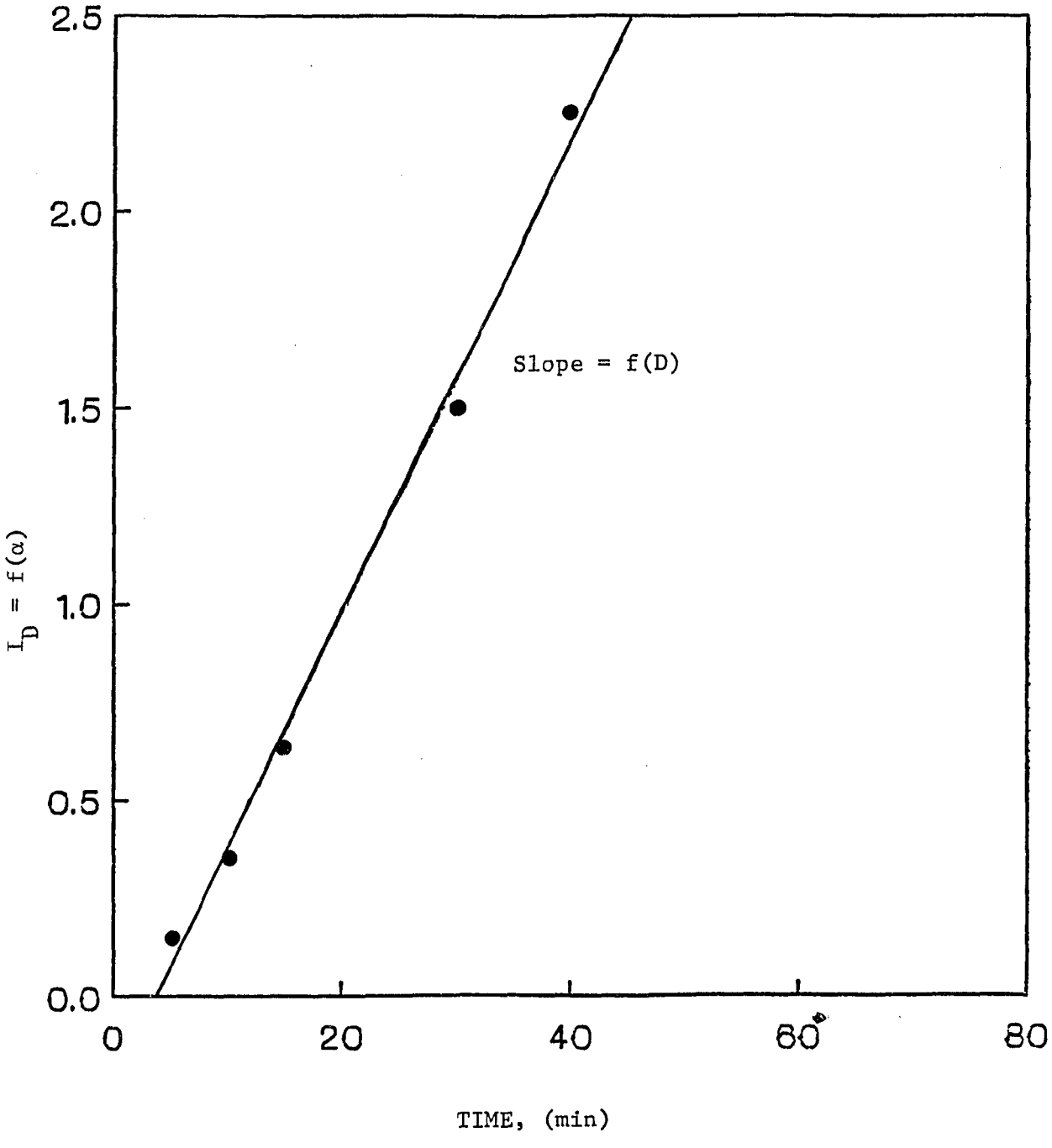

Figure 8. Plot of diffusion chronomal, I_D, versus time

to the slope of I_D versus t plot and estimated to be about 10^{-6} cm^2/sec, which is about an order of magnitude less than that of ionic species in aqueous solutions. Such a low diffusion coefficient confirms that the growth of the spherical particles proceeds by diffusion of crystallites through the depleted aqueous layer. Similar observations were reported by Bleier and Cannon [12] for formation of uniform m-ZrO_2 particles and by Edelson and Gleaser [13] for spherical TiO_2 particles.

Formation of monosize particles at moderate rates may be explained in light of the above agglomeration mechanism. If the rate of crystallite generation is comparable to that of diffusion of these crystallites to deposit on the growing agglomerate, then the agglomerates will grow uniformly to produce monosized particles. If on the other hand, the crystallite generation rate is higher than the diffusion rate, then the population of these crystallites may reach a critical value at which second generation of particles form, resulting in a bimodal size distribution. Figure 9 shows schematically the formation mechanism for bimodal size distribution. Figure 9(a) represents the formation of crystallites in the solution. High concentration of crystallites results in agglomeration of nearly uniform size spherical particles as predicted by estimated agglomeration rate (Figure 9(b)). Broken circles around each agglomerate represent the aqueous layer with depleted crystallite concentration. Since the sulfide ion generation rate is quite high, a large number of new crystallites form throughout the solution.

Figure 9. Schematic diagram of mechanism of particle formation and growth for a case yielding a bimodal size distribution

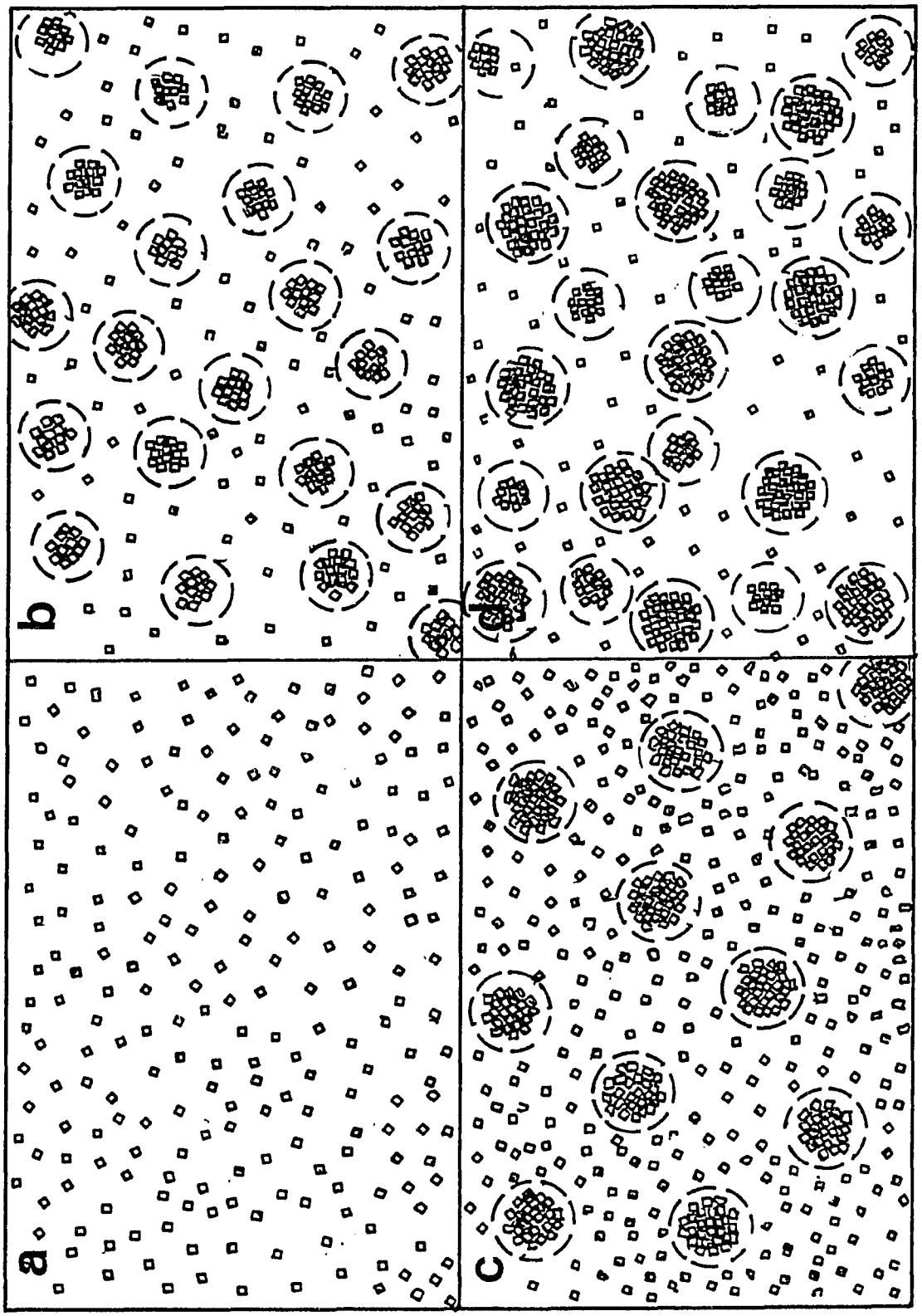
b
a
c

The crystallite population outside the layer builds up, while those crystallites that form within the layer contribute to the growth of agglomerates (Figure 9(c)). As soon as the crystallite concentration outside the layer reaches a critical value, a second agglomeration event takes place, resulting in a second generation of agglomerates which are smaller than the first generation, as shown in Figure 9(d). A very high percentage of crystallites forming afterwards is consumed in the growth process due to the large number of growing agglomerates. Depending on the sulfide ion generation rate, it is possible that multiple agglomeration events may occur resulting in a wide particle size distribution, as is shown in Figure 6.

CONCLUSIONS

The formation of uniform spherical particles of ZnS was investigated, with primary consideration being given to the influence of experimental variables on the morphology. It was determined that nucleation starts at a constant supersaturation level of 8.5 for a number of combinations of experimental variables. Type of particle size distribution was found to be controlled by the rate at which this critical nucleation event is reached (i.e., the rate-to-nucleation), irrespective of the value of the individual variables.

The mechanism of particle formation is believed to follow a two-step process with the formation of nuclei of about 15 nm size, and then, aggregation of these crystallites to form spherical particles consisting of clusters of about 0.3 to 1.0 μm size. The type of the particle size distribution was controlled by two competing processes: 1) rate of sulfide ion generation, and 2) rate of growth of agglomerates. Spherical submicron ZnS powders with desired size distribution were produced reproducibly by controlling the rate of sulfide ion generation.

REFERENCES CITED

1. P. A. Miles, J. Opt. Soc. Am. 63, 1323 (1973).

2. H. W. Leverenz, Science 109, 183 (1929).

3. G. Chiu, J. Coll. and Int. Sci. 83 [1], 309 (1981).

4. D. M. Wilhelmy and E. Matijevic, J. Chem. Soc., Faraday Trans. 1 80, 563 (1984).

5. R. Williams, P. N. Yocom and F. S. Stofko, J. Coll. and Int. Sci. 106 [2], 388 (1985).

6. E. H. Swift and E. A. Butler, Anal. Chem. 28 [2], 146 (1956).

7. D. C. Harris, Quantitative Chemical Analysis, 2nd Edition (W. H. Freeman and Company, New York, 1987), pp. 725-726.

8. A. Celikkaya and M. Akinc, unpublished work, Department of Materials Science and Engineering, Iowa State University, Ames, IA.

9. V. K. LaMer and R. J. Dinegar, Am. Chem. Soc. 73, 3280 (1951).

10. M. Akinc, Proposal submitted to the Office of Naval Research, Arlington, VA, 1986.

11. A. E. Nielsen, Kinetics of Precipitation (The Macmillan Company, New York, 1964), pp. 29-39.

12. A. Bleier and R. M. Cannon, in Better Ceramics Through Chemistry II, edited by C. J. Brinker, D. E. Clark and D. R. Ulrich (Materials Research Society, Pittsburgh, PA, 1986), p. 71.

13. L. H. Edelson and A. M. Gleaser, J. Am. Ceram. Soc. 71 [4], 225 (1988).

ACKNOWLEDGMENTS

This work was supported in part by the Office of Naval Research and by Iowa State University. The authors are grateful to Professor M. F. Berard for critical review and Ms. Lynne Gaskill for typing the manuscript.

SECTION II. MORPHOLOGY OF ZnS PARTICLES PRODUCED FROM VARIOUS ZINC SALTS BY HOMOGENEOUS PRECIPITATION

ABSTRACT

Colloidal sols of ZnS were prepared by thermal decomposition of thioacetamide in acidic zinc solutions. Precipitation was carried out in the presence of nitrate, acetate, chloride and sulfate ions. Particle morphology was influenced by the chemical nature of the anions present in the solution, as well as the rate of sulfide ion generation. Spherical, monodisperse particles having a specific type of particle size distribution, i.e., monosized, bimodal or continuous distribution, with mean sizes in the range of 0.15 μm to 3 μm, were formed depending on the anion type and sulfide ion generation rate. Individual particles always consisted of clusters of sphalerite crystallites, except when sulfide ions were generated at low rates and sulfate ions were present. In such cases, a mixture of α and β-ZnS was formed.

INTRODUCTION

Over the past decade, several researchers have produced colloidal sols of many hydrous oxides and sulfides consisting of particles having uniform size and shape. In addition to the commonly recognized variables such as pH, temperature and concentrations of various chemical reactants, the type of the electrolyte present can significantly affect system stability, particle morphology and composition of the precipitate through complex formation. Complexing of the precipitating cation with one or more of the anions present in the system, at varying strengths, may either limit the concentration of free cations in the solution or serve as an intermediate species contributing to the formation of a particular crystalline phase and/or particle morphology. Alternatively, those anions acting as a weak base may buffer the pH of the solution leading to similar results. It is also possible that these anions may be incorporated into the solid phase, affecting the composition of the precipitates.

Although considerable progress has been made in explaining various aspects of the precipitation phenomena, it is difficult to draw general conclusions from specific systems. However, demonstration of the ability to reproducibly prepare colloidal particles of a specific composition and morphology under various experimental conditions can lead to models which can lead to further understanding of the precipitation phenomenon.

Studies dealing with the synthesis and characterization of colloidal sols of oxides, carbonates, phosphates, and their combinations are more common in the literature than those concerned with nonoxide salts, such as sulfides, selenides and others. This is very probably due to toxicity problems and/or the sensitivity of the nonoxide reactants and products to air and water vapor [1, 2]. Wilhelmy and Matijevic [3] prepared spherical, micron sized β-ZnS particles by aging zinc ions in hot thioacetamide solution for several hours, with nitrate being the supporting anion. Williams et al. [4], on the other hand, used sulfate as the supporting anion to prepare 3 μm zinc sulfide spherical particles which were a mixture of the α and β forms. Williams et al. [4] reported that the spheres initially appeared as cubes of 1 μm size, while Wilhelmy and Matijevic [3] observed 0.16 μm spherical "seeds" initially.

The primary purpose of the present study was to investigate the role of supporting anions on the kinetics of precipitation and on the morphology of the particles formed. To do this, zinc sulfide was precipitated by thermal decomposition of thioacetamide (TAA) in acidic aqueous solutions where sulfate, acetate, chloride and nitrate ions were employed as supporting anions.

Precipitation of zinc sulfide by thermal decomposition of TAA in acidic solutions is known to proceed as follows [5, 6]:

$$CH_3C(S)NH_2 \xrightarrow{H_3O^+} CH_3C(O)NH_2 + H_2S \qquad -\frac{d[TAA]}{dt} = k[H_3O^+][TAA] \qquad (1)$$

$$H_2S \rightleftharpoons HS^- + H_3O^+ \qquad K_{a,1} = \frac{[HS^-][H_3O^+]}{[H_2S]} \tag{2}$$

$$HS^- \rightleftharpoons S^= + H_3O^+ \qquad K_{a,2} = \frac{[S^=][H_3O^+]}{[HS^-]} \tag{3}$$

$$Zn^{2+}(aq) + S^=(aq) \rightleftharpoons ZnS(s) \qquad K_{sp} = [Zn^{2+}][S^=] \quad . \tag{4}$$

Decomposition of TAA to yield hydrogen sulfide is the rate limiting step, and the decomposition kinetics have been studied in great detail [5]. Using Eqs. (1-3), the sulfide ion concentration at any time (t) can be estimated for any combination of pH, temperature, and initial concentration of thioacetamide. Then, it is possible to determine the supersaturation (S), defined as

$$S = \left(\frac{[S^=]_t [Zn^{2+}]}{K_{sp}} \right)^{1/2} \quad , \tag{5}$$

at the instant of nucleation, where t is the observed time from the beginning of the experiment to the onset of nucleation, K_{sp} is the equilibrium solubility product of β-ZnS, $[Zn^{2+}]$ is the concentration of free zinc ions and $[S^=]_t$ is the concentration of sulfide ions at time (t) given by [7]:

$$[S^=]_t = \frac{[TAA]_0 (1-\exp(-k[H_3O^+]t))}{([H_3O^+]^2/K_{a,1}\ K_{a,2}) + ([H_3O^+]/K_{a,2}) + 1} \quad . \tag{6}$$

Thus, one can estimate the degree of supersaturation for nucleation using Eqs. (5) and (6).

EXPERIMENTAL

Precipitation

Stock solutions of zinc acetate, zinc sulfate, zinc chloride and zinc nitrate (Fisher reagent grade) were prepared by dissolving each salt in deionized water so as to produce a zinc ion concentration about 1.5 M. Solutions were filtered through 0.1 μm membranes and stored in polyethylene bottles. Cation stock solution and the conjugate acid of the supporting anion were added to a beaker in predetermined quantities along with a sufficient amount of distilled water to bring the total volume slightly less than 250 mL. The amount of the acid and cation stock solutions added were determined on the basis of desired pH and cation concentration. The acidic cation solution was heated to reaction temperature on a hot plate, and the predetermined amount of thioacetamide (Aldrich Chemical Company) was dissolved in the solution. Solution volume was brought to exactly 250 mL, and the beaker containing the solution was placed in a water bath at the set reaction temperature. The time to onset of precipitation, manifested as the appearance of a bluish tint, was recorded for each experiment. Small aliquots were collected and quenched to 15°C at regular intervals to observe development of particle morphology and growth kinetics.

Initial zinc ion concentration, $[Zn^{2+}]_0$, was kept constant at 0.05 M in all experiments, while initial thioacetamide concentration was varied to give $[TAA]_0/[Zn^{2+}]_0$ ratios of 4, 8, and 16. Two levels

of solution pH were obtained with conjugate acids (pH = 1 and pH = 2). When the supporting anion was acetate, however, the pH of the system remained constant at 1.9, possibly due to buffering action of the acetate ions with other ions in the solution.

Characterization

A centrifugal particle size analyzer[1] was employed for the determination of size distribution using a portion of quenched aliquots. The remainder of each aliquot was centrifuged at 5000 rpm for 45 min. The recovered precipitates were then washed once with deionized water and once with acetone. During the acetone wash, particles were dispersed with a sonic disruptor[2]. A drop of suspension in acetone was placed on an aluminum foil and dried for observation of morphology by SEM[3]. X-ray diffraction[4] patterns were obtained to determine the structure, mean crystallite size and phase purity of the powders. Organic contaminants were assessed from FTIR[5] spectra.

---

[1]Horiba particle size analyzer, CAPA 700, Horiba Co., Irvine, CA.

[2]Tekmar sonic disruptor, Tekmar Company, Cincinnati, OH.

[3]JEOL Model 840A, JEOL, Ltd., Peabody, MA.

[4]Siemens D500 diffractometer, Siemens Company, Denver, CO.

[5]IBM IR 98 FTIR spectrophotometer, IBM Instruments, Inc., Danbury, CT.

RESULTS AND DISCUSSION

Effects of Supporting Anion on Precipitation Kinetics

The critical supersaturation was determined for a number of combinations of experimental variables, and was found to have a value of about 8.5 for any combination of experimental variables. Figure 1(a) shows the change of supersaturation S with time plotted using Eqs. (5) and (6) for temperature T = 60°C, initial thioacetamide concentration $[TAA]_0$ = 0.4 M, pH = 2, and initial zinc ion concentration $[Zn^{2+}]_0$ = 0.05 M, assuming that all zinc ions are free. On the same figure, the times to observe the onset of the precipitates are indicated with corresponding values of critical supersaturation for each anion system. The kinetics of the formation of spherical submicron ZnS particles with nitrate as the supporting anion have been previously reported [8]. Since nitrate ions do not form strong complexes with Zn^{2+} [9], variations in precipitation kinetics and particle characteristics observed with other supporting anions were compared to those for nitrate in this study. Two possible explanations can be offered for the observed variation in the value of critical supersaturation for different anion systems. First, the presence of a specific anion may effectively alter the solid-liquid interfacial energy which would cause the critical nucleus size to be different for each anion system. This is equivalent to saying that the critical supersaturation is indeed different for each anion system. Secondly, it is also possible that although the critical supersaturation is the same for each anion

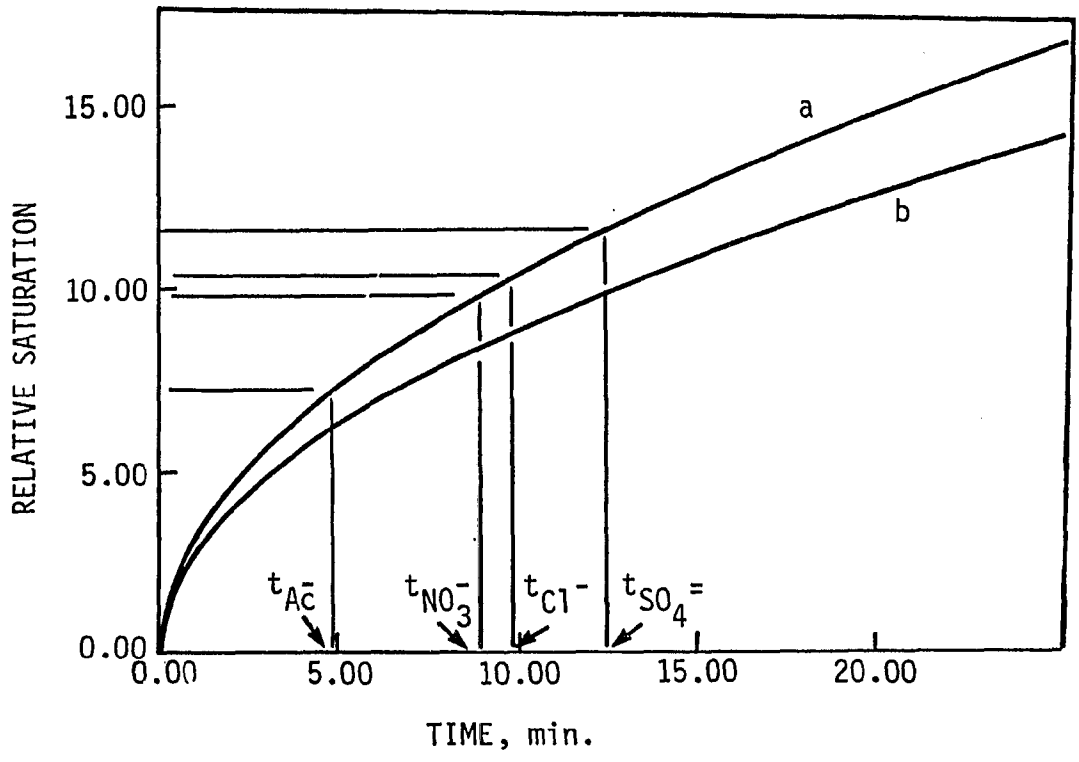

Figure 1. Change of relative supersaturation with time where $T = 60°C$, $[TAA]_o = 0.4$ M, pH = 2 and a) $[Zn]_o = 0.05$ M and b) $[Zn]_o = 0.0425$ M. Times to observe nucleation are indicated with corresponding values of critical relative saturation for acetate, nitrate, chloride and sulfate solutions

system, nucleation starts at different times because a certain fraction of the initial zinc ions may be complexed by anions in the solution. Table 1 lists the formation constants for acetato, sulfato, chloro and nitrato complexes of zinc corrected for the ionic strengths of the solutions that we used [9]. Complex species involving hydroxide ions were not considered since they are known not to be significant below pH = 3 [10], and all of our experiments were performed with pH at or below 2.

Taking into consideration the buffering effect of HSO_4^- and $SO_4^=$ ions at a pH of 2 and the expected complex formation reactions, we calculated that about 15% of the Zn^{2+} ions will be tied up by sulfate ions. Similar calculations indicate that only 4% of the Zn^{2+} ions will be complexed by nitrate ions, validating the assumption that nitrate can be considered inert in terms of complex forming ability.

Table 1. Concentration equilibrium constants for acetato, nitrato, sulfato and chloro complexes of Zn^{2+} ions found by interpolation using Davies equation at corresponding ionic strengths of the solutions used in this study

Formation constant	Ligand (L^{-y})			
	$SO_4^=$	OAc^-	NO_3^-	Cl^-
$K_{f,1}$ $[ZnL_1]^{-y+2}$	12.58	11.22	0.66	2.32
$K_{f,2}$ $[ZnL_2]^{-2y+2}$	7.94	6.16	0.38	1.41
$K_{f,3}$ $[ZnL_3]^{-3y+2}$	0.70	1.23	--	0.89
$K_{f,4}$ $[ZnL_4]^{-4y+2}$	1.13	--	--	0.50

The predicted influence of sulfate complexing of zinc ion on the supersaturation with time is shown as curve b in Figure 1, where a 15% reduction in $[Zn^{++}]_0$ (from 0.050 M to 0.425 M) has been assured because of complexing. The time for critical supersaturation of $S \simeq 8.5$ is read from curve b as 13 min, which is slightly longer than that found experimentally. This small difference may be due to uncertainties involved in determining the exact time at which nucleation started; however, this analysis is consistent with the delay in nucleation for the sulfate system due to lower free zinc ion concentration. Calculations for the chloride system also supported this conclusion. Although stability constants for acetato complexes of zinc (Table 1) are very close to those for sulfato complexes, nucleation is observed in the acetate system much earlier than for sulfate and even nitrate. Obviously, the presence of acetate ions either catalyses the thioacetamide decomposition or helps to reduce critical nucleus radius. The latter mechanism is possible if acetate reduces the surface energy of the nuclei or forms intermediate species that facilitate attachment of ions to subcritical nuclei. Figure 2 shows the variation of thioacetamide concentration with time. Curve a is obtained from Eq. (1) and curve b corresponds to experimentally measured values as determined by following the concentration of TAA at 261 nm by a UV-Vis spectrophotometer in the presence of zinc and acetate ions. The apparent sudden increase in TAA concentration measured experimentally is actually due to scattering by the formation of precipitate particles rather than to an abrupt change in TAA

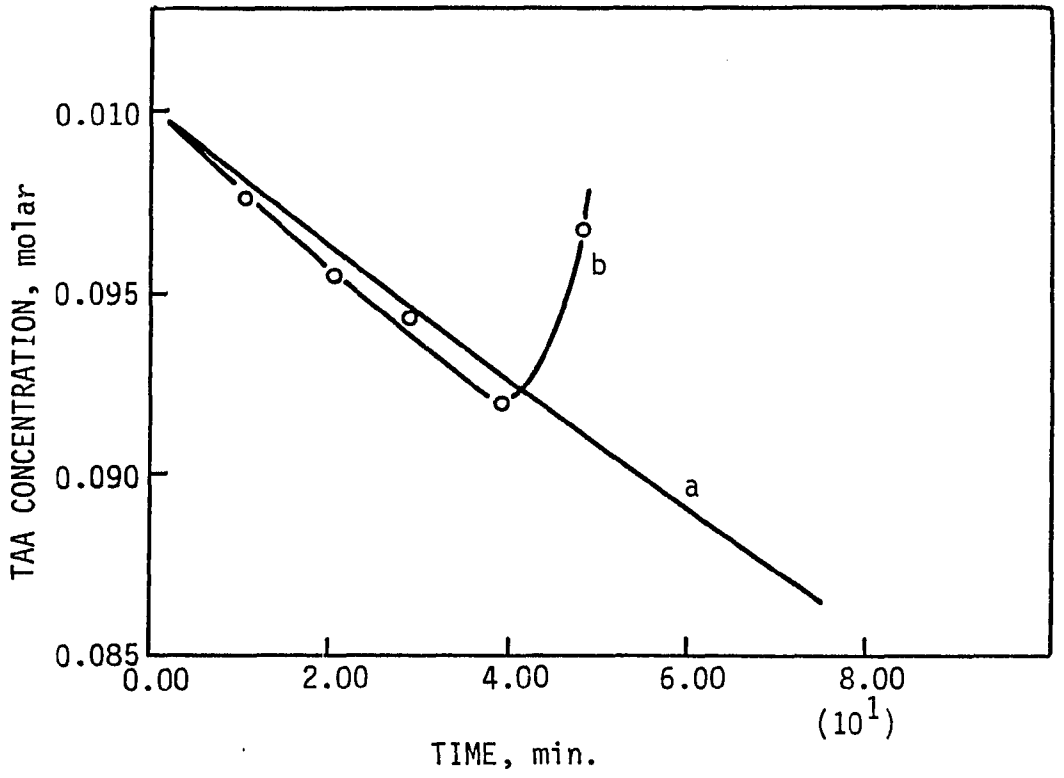

Figure 2. Variation of concentration of thioacetamide as determined a) theoretically and b) experimentally at pH = 2, $[TAA]_o$ = 0.1 M, T = 60°C

concentration. Since the experimental data follow the theoretical curve very closely prior to precipitation, the premise that the presence of acetate ions augments the rate of decomposition of TAA fails. FTIR spectra of ZnS powders prepared from acetate solutions did not contain any peaks indicating involvement of an intermediate species in the solid phase. Thus, it is difficult to explain the observed anomalously early nucleation from acetate solutions, and this phenomenon needs to be investigated in more detail.

Effect of Supporting Anion on Particle Morphology

Nitrate system

The size distribution type and texture of particles varied considerably with the chemical nature of the supporting anions present and with the sulfide ion generation rate. As has been discussed, the sulfide ion generation rate is a function of temperature, pH and initial concentration of thioacetamide; thus, all of these variables determine the rate of approach to critical supersaturation. Since critical supersaturation was observed to be approximately the same for all experiments, the reciprocal of time at which nucleation was observed represents a sort of averaged rate of approach to nucleation and will be referred to as "rate-to-nucleation". Rate-to-nucleation (RN) for various combinations of experimental variables for nitrate solutions are given in Table 2. Below RN = 1.11×10^{-2} min^{-1}, it usually took exceedingly long times for precipitation to start (~3 hours) and agglomerates of particles were observed. However,

Table 2. Variation of rate of sulfide ion generation with various combinations of experimental parameters for nitrate system $[Zn^{2+}]_0$ = 0.05 M

Temperature (°C)	pH	$[TAA]_0$	RN (min^{-1})
60	1	0.2	6.6×10^{-3}
60	1	0.4	1.41×10^{-2}
70	1	0.2	2.70×10^{-2}
70	1	0.4	5.88×10^{-2}
70	1	0.8	1.11×10^{-2}
70	2	0.2	0.250
70	2	0.4	0.500
70	2	0.8	1.00
80	2	0.2	1.50
80	2	0.4	3.00

depending on the relative value of RN above 1.11×10^{-12} min^{-1}, either monosized, bimodal or continuous distributions of particle sizes were obtained with the nitrate system. Monosized particles were observed for RN in the range of 1.11×10^{-2} min^{-1} to 1.00 min^{-1} (Figure 3(a)). At intermediate RN values ($1.00 < RN < 1.50$ min^{-1}), bimodal particle size distributions were obtained (Figure 3(b)). At still higher RN values, continuous particle size distributions were obtained (Figure 3(c)). (Figure 3(c)). The variation of type of particle size distribution with RN is related to rate of sulfide ion generation and its consumption in the growth process [8].

X-ray diffraction spectrum of the ZnS procedure produced from nitrate solutions is given in Figure 4. The pattern is that of sphalerite [11], and there is no evidence of existence of any other crystalline phase. Crystallite size was determined to be on the order of 15 nm by the X-ray line broadening technique, indicating the polycrystalline nature of spherical particles.

Sulfate system

ZnS particles formed in sulfate solutions were significantly different in morphology than those formed in nitrate solutions. At low RN values, spherical monosized polycrystalline particles of about 3 μm in diameter were formed, as shown in Figure 5. X-ray diffraction patterns indicate that the powders consist of both α and β forms of ZnS. No attempt was made to determine the microscopic distributions and the relative amounts of these two phases. The fibrous texture observed for these particles is believed to be due to nuclei that

Figure 3. Scanning electron micrographs of ZnS powders obtained from nitrate solutions with $[Zn^{+2}]_o$ = 0.05 M, pH = 2 and

a) T = 70°C, $[TAA]_o$ = 0.8 M,
b) T = 80°C, $[TAA]_o$ = 0.2 M,
c) T = 80°C, $[TAA]_o$ = 0.4 M

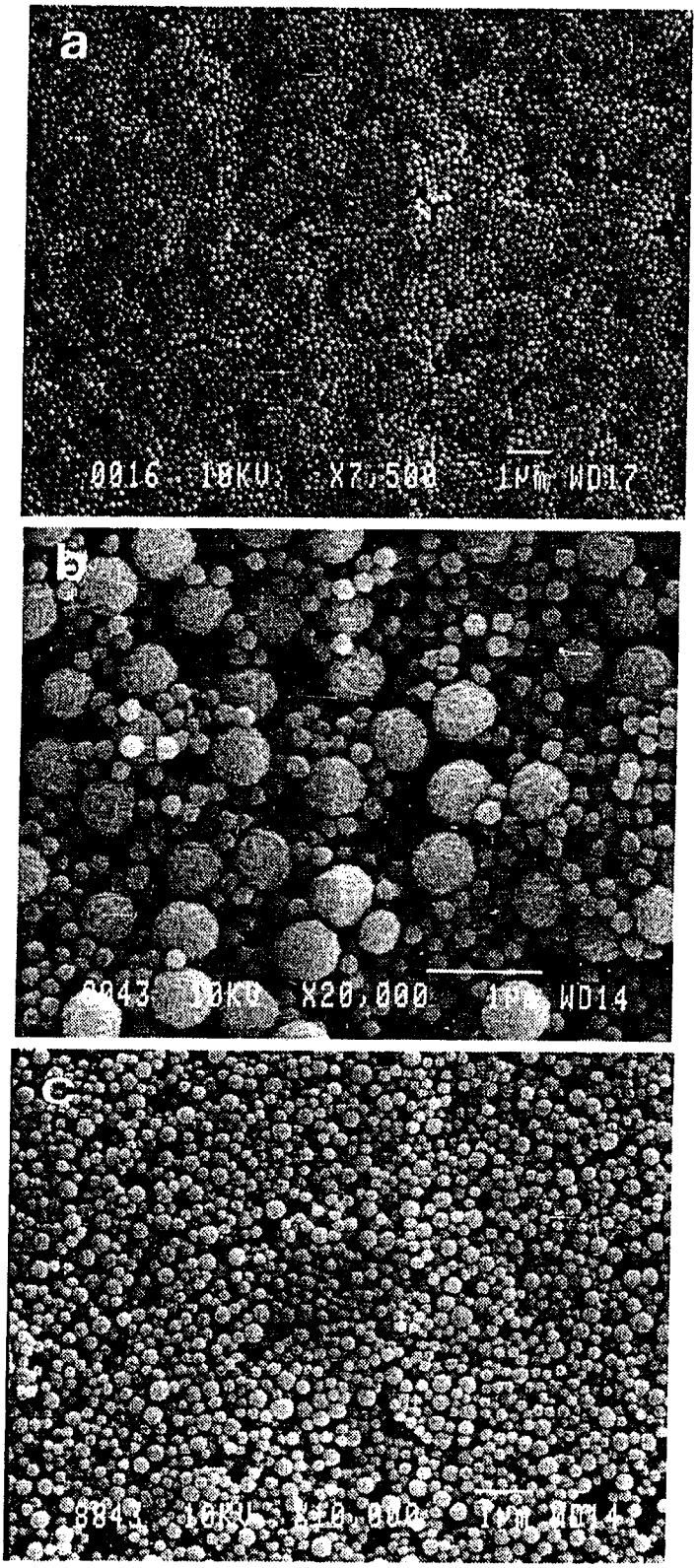
a
0016 10KV X7,500 1μm WD17
b
0043 10KV X20,000 1μm WD14
c

Figure 4. XRD trace of ZnS powders prepared from nitrate solutions

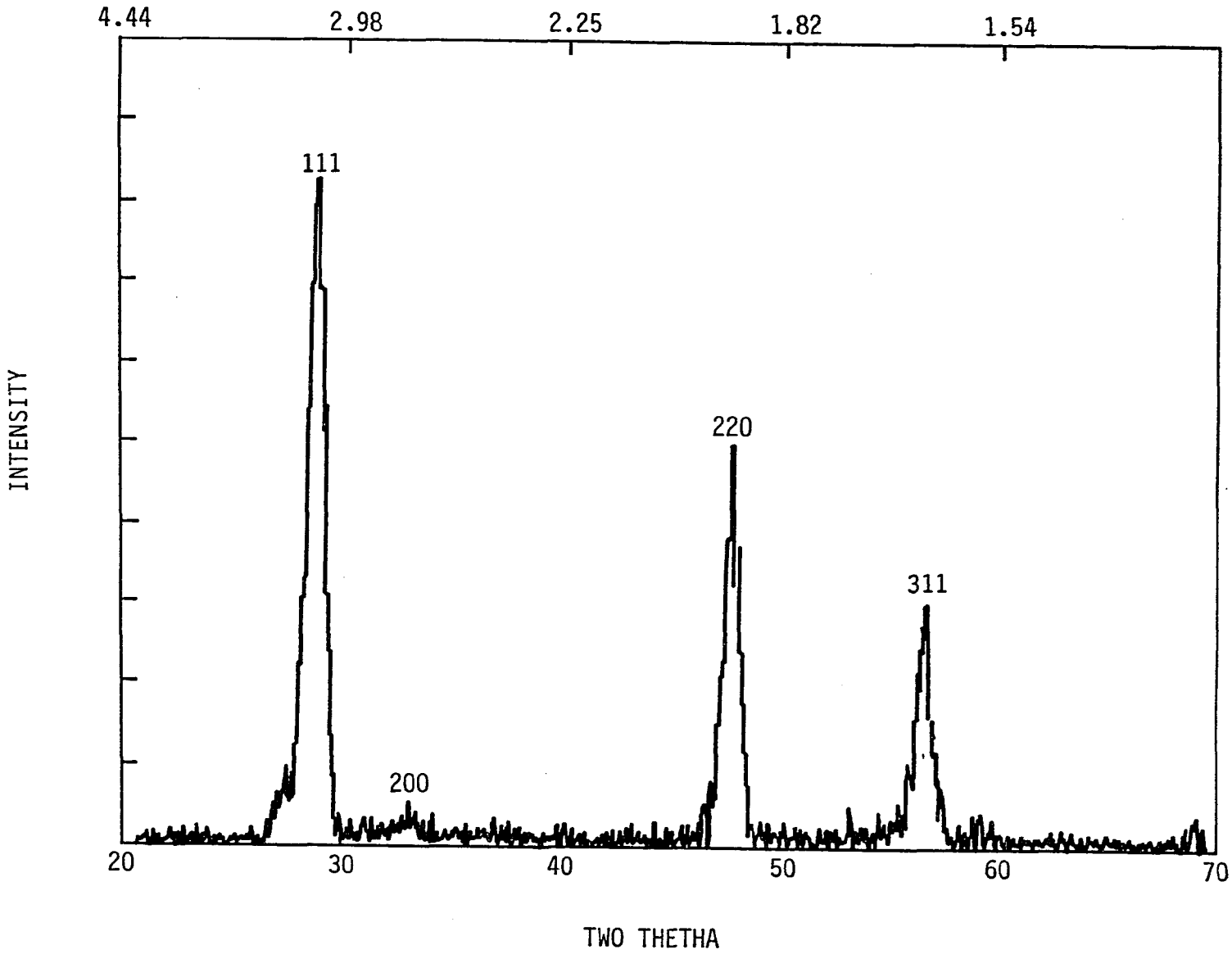
4.44
2.98
2.25
1.82
1.54
111
200
220
311
INTENSITY
20
30
40
50
60
70
TWO THETHA

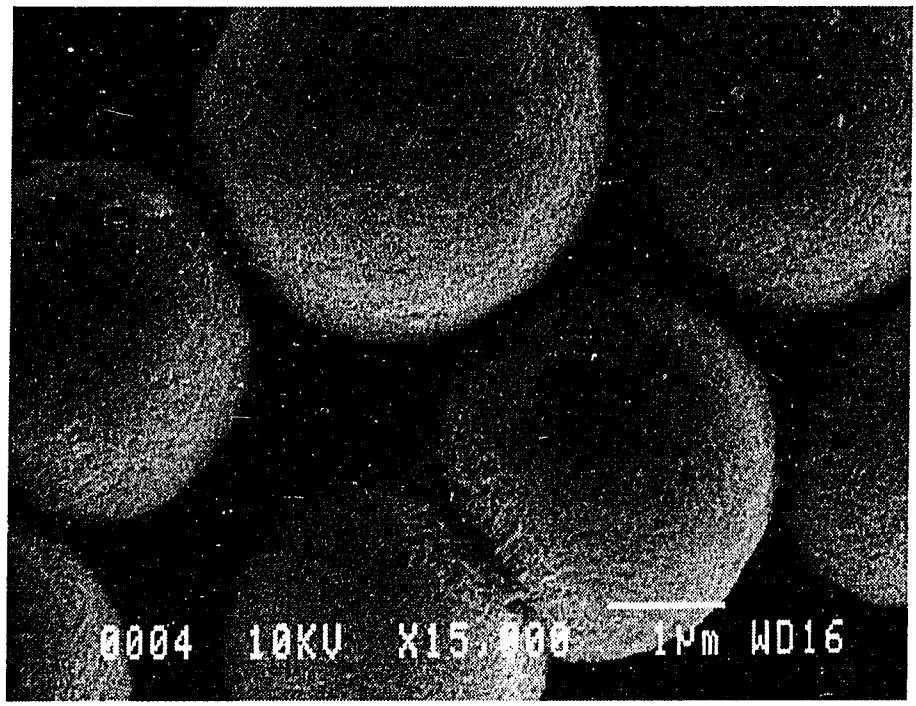
0004 10KV X15,000 1μm WD16

elongated before they attached onto the surface of the growing particles. Similar texture and particle morphology were observed by Williams et al. [4]. However, they claimed that particles formed by first forming faceted 1 μm cubic crystals followed by the deposition of fibrous crystallites onto the primary crystal. Contrary to their proposed mechanism, we have not seen any primary crystals in the micron size range. At higher RN values, a second generation of particles appeared after first generation particles reached a diameter of about 3.5 μm, as is shown progressively in Figure 6. Eventually, the second generation particles grew to diameters of 1-2 μm (Figure 6(c)). It is interesting to note that fibrous textures were more apparent in the second generation of particles, and that the resulting particles were highly agglomerated (Figure 6(d)). Another significant observation was that at high RN values, only the β phase (sphalerite) was formed, which suggests that the fibrous features may be associated with the β phase.

Chloride system

Particles from chloride solutions were very similar to those from nitrate solutions in the range $0.25 < RN < 1.0$ min^{-1}. Monosized, spherical particles with growth rates very similar to those from nitrate solutions were obtained in this range. Figure 7(a) shows a micrograph of ZnS particles prepared in the presence of chloride ions at a temperature of 70°C, pH = 2, $[Zn^{2+}]_o$ = 0.05 M and $[TAA]_o$ = 0.8 M (RN = 1.00). At higher RN values, unlike the nitrate results, chloride solutions did not yield either bimodal or continuous size distributions, probably because the effective zinc ion concentration in

Figure 6. Scanning electron micrographs of ZnS powders from sulfate solutions a) 15, b) 30, c) 60, and d) 90 min. after precipitation started with T = 70°C, pH = 2, $[TAA]_o$ = 0.4 M and $[Zn^{2+}]_o$ = 0.05 M

a
00 4 10KV X10,000 1μm WD16
b
0006 10KV X10,000 1μm WD16
c
0007 10KV X10,000 1μm WD16
d
0009 10KV X10,000 1μm WD16

Figure 7. Scanning electron micrographs of ZnS particles obtained from chloride solutions at pH = 2, $[Zn^{2+}]_o$ = 0.05 M, $[TAA]_o$ = 0.8 M, and a) T = 70°C, b) T = 80°C

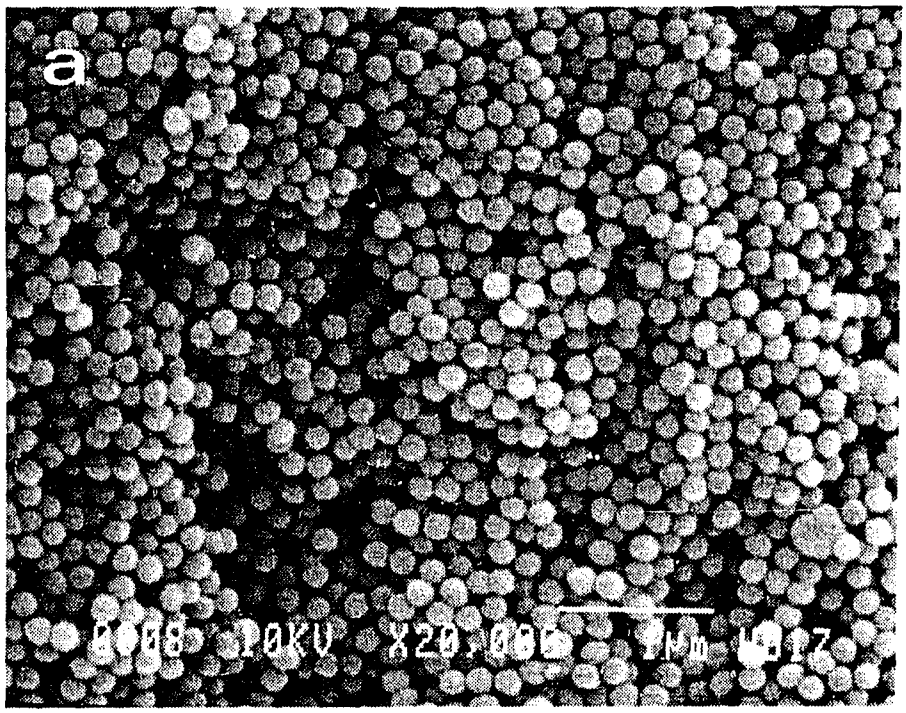
a
10KV
1μm

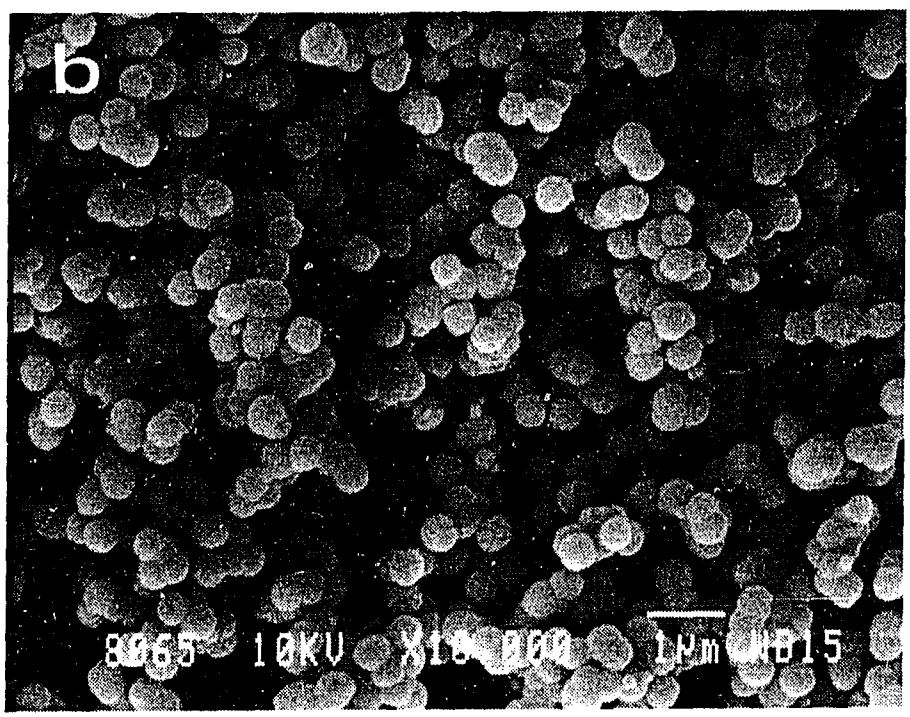
b
10KV
1μm

the solution was diminished by formation of chloride complexes. Instead, highly agglomerated particles having an average diameter of about 1 μm were obtained, as shown in Figure 7(b).

Acetate system

Particle morphology showed only a slight dependence on RN when prepared from acetate solutions. Spherical monosized particles of β-ZnS were obtained with all combinations of experimental variables investigated. Because of buffering, the pH remained fixed at 1.9 and therefore, could not be treated as a variable. Figure 8 shows particles 60 min. after the onset of nucleation under various experimental conditions. A shift in mean particle diameter to a larger size is obvious as RN gets lower.

The substructure of particles obtained from acetate solutions was very similar to that from nitrate solutions, i.e., aggregates of nanometer-sized crystallites, as determined from X-ray diffraction line broadening and verified by a specific surface area of about 55 m^2/gr.

Although the low value of S indicates that nucleation kinetics were accelerated in the presence of acetate ions, the growth rate was significantly reduced compared to other anion systems. For example, it took about three hours after nucleation for the particles in Figure 8(a) to reach a diameter of 0.25 μm.

Figure 8. Scanning electron micrographs of powders obtained from acetate solutions 60 min. after nucleation at $[Zn^{2+}]_o$ = 0.05 M, pH = 2 and

a) T = 80°C, $[TAA]_o$ = 0.4 M
b) T = 60°C, $[TAA]_o$ = 0.8 M
c) T = 60°C, $[TAA]_o$ = 0.2 M

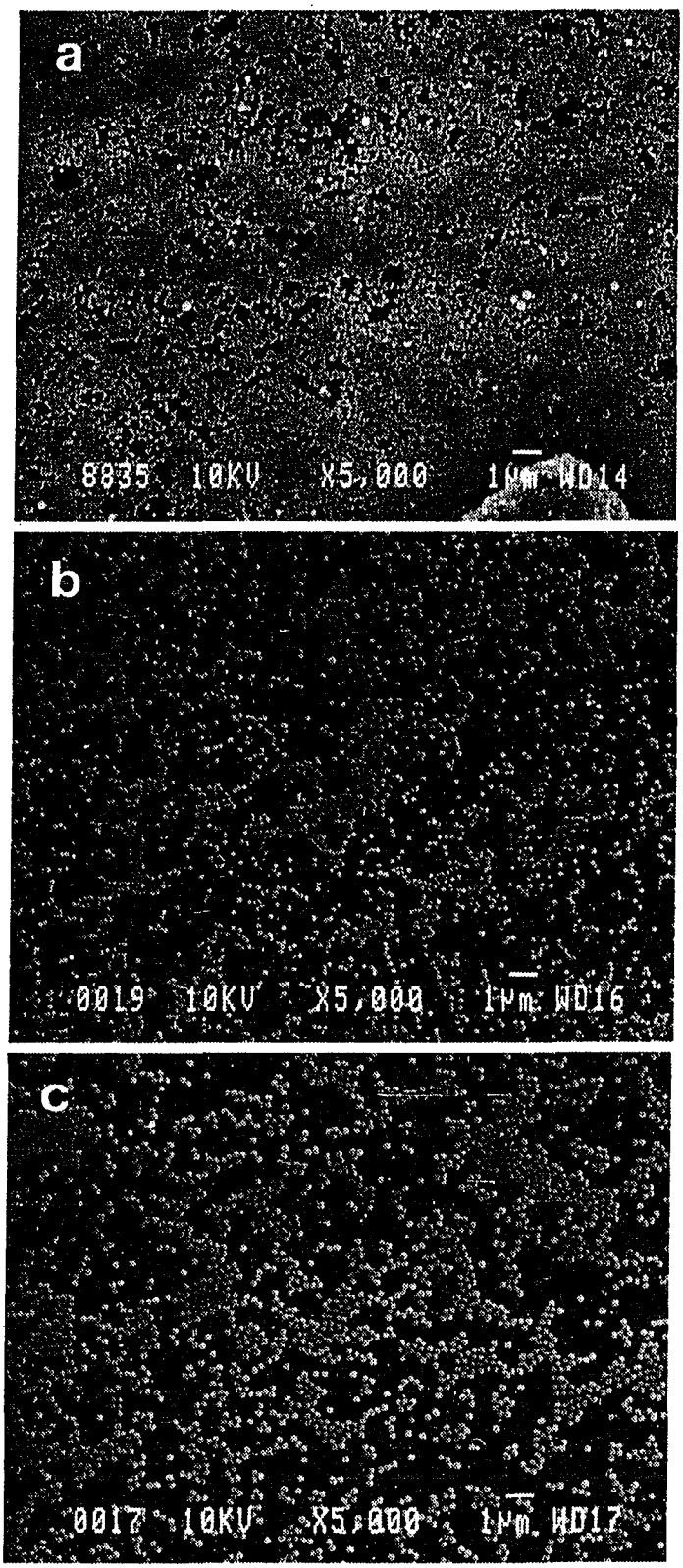
a
8835 10KV X5,000 1μm WD14
b
0019 10KV X5,000 1μm WD16
c
0017 10KV X5,000 1μm WD17

CONCLUSIONS

Mean ZnS particle size and distribution were affected by the sulfide ion generation rate for all supporting anions except acetate. Depending on the sulfide ion generation rate, monosized, bimodal or continuous size distribution was observed. Nitrate, chloride and acetate solutions produced submicron size particles in the range of variables studied, while sulfate ion solutions produced particles up to 3 μm in diameter. Sulfate ion solutions produced particles that had a fibrous texture which was not apparent in other systems. The unique morphology of the particles produced in the presence of sulfate ions was attributed to complexing of zinc ions with sulfate, thus reducing the rate of nuclei formation compared to other systems. The attachment of sulfate ion onto the growing nuclei to modify the growth habit also cannot be ruled out. Acetate solutions produced very fine (0.1 - 0.25 μm) spherical monosize particles over a wide range of experimental conditions. Acetate ions appeared to hasten nucleation, yet growth was slow compared to other systems. This phenomenon was attributed to association of acetate and zinc ions to reduce nucleation barrier, resulting in rapid nucleation, but little growth.

Powder morphology was more easily controlled in nitrate solutions than with other supporting anions, and the powder characteristics obtained, i.e., size distribution and phase purity, were considered superior to powders obtained with the other anions.

REFERENCES CITED

1. E. Matijevic, J. Coll. Int. Sci. 58 [2], 374 (1977).

2. E. Matijevic, in Ultrastructure Processing of Ceramic Glasses and Composites, edited by L. L. Hench and P. R. Ulrich (John Wiley and Sons, Inc., New York, 1984).

3. D. M. Wilhelmy and E. Matijevic, J. Chem Soc. Faraday Trans. 80, 563 (1984).

4. R. Williams, P. N. Yocom and F. S. Sotofko, J. Coll. Int. Sci. 106 [2], 388 (1985).

5. E. H. Swift and E. A. Butler, Anal. Chem. 28 [2], 146 (1956).

6. D. M. King and F. C. Anson, Anal. Chem. 33 [4], 573 (1961).

7. M. Akinc, Research Proposal submitted to the Office of Naval Research, Arlington, VA, 1986.

8. A. Celikkaya and M. Akinc, Submitted to J. Coll. Int. Sci. (1988).

9. S. Kotrly and L. Sucha, Handbook of Chemical Equilibria in Analytical Chemistry (Ellis Hornwood Limited, West Sussex, England, 1985), pp. 143-208.

10. A. O. Gubeli and J. Ste-Marie, Can. J. Chem. 45, 2101 (1967).

11. JCPDS X-ray Powder Diffraction File, No. 5-566.

ACKNOWLEDGMENTS

This work was supported in part by the Office of Naval Research and by Iowa State University. The authors are grateful to Professor M. F. Berard for critical review and Ms. Lynne Gaskill for typing the manuscript.

SECTION III. HOT PRESSING OF ZnS POWDERS WITH SUBMICRON PARTICLES

NOMENCLATURE

A	=	Dorn constant
b	=	Burger's vector
D	=	Percent relative density
D_b	=	Boundary diffusion coefficient
D_v	=	Volume diffusion coefficient
G	=	Average grain size
k	=	Boltzmann constant
n	=	Stress exponent
P	=	Applied pressure
P_{eff}	=	Effective pressure
R	=	Initial particle size
r	=	Pore radius
T	=	Absolute temperature
x	=	Radius of neck area
ρ	=	Relative density
ρ_o	=	Initial relative density
μ	=	Shear modulus
δ	=	Boundary thickness
γ	=	Curvature of neck
Ω	=	Atomic volume

ABSTRACT

The hot-pressing behavior of spherical, submicron size ZnS powders was investigated between 800 and 900°C at pressures from 7 to 105 MPa at various times. The influence of temperature, pressure and time on density and on the microstructure of the hot-pressed specimens was studied.

Densification maps were prepared and the dominant densification mechanisms were identified for a number of combinations of experimental parameters at various stages of the hot-pressing process.

INTRODUCTION

Polycrystalline zinc sulfide is used as a window material for applications requiring transmission in the 8-12 μm region of electromagnetic spectrum. Optical and thermomechanical properties of ZnS form a baseline against which other high temperature, long wavelength infrared-transmitting materials are compared. An optimum combination of thermomechanical and optical properties can only be obtained with fully-dense, fine-grained and uniform microstructures. The manufacture of components with this kind of microstructure constitutes the goal of most of the current research in ceramic processing.

The high degree of covalent bonding, i.e., low atomic mobility, involved in ZnS requires relatively higher temperatures and/or excessively long times to achieve extensive densification by ambient pressure sintering. Due to its high vapor pressure at such elevated temperatures, ZnS does not lend itself to normal sintering. High sintering temperatures and/or long sintering times can be avoided by using additives that promote densification. McQueen and Kuczynski [1] studied sintering of Ag-doped ZnS at 900°C for 100 hours. The resulting density was 98% of theoretical. Fujita and Nitta [2] studied the effects of alkali and alkaline-earth chloride additives on the sintering of ZnS powder compacts in a flowing H_2S atmosphere. $BaCl_2$ was found to promote the sintering of ZnS by forming a compound Ba_2ZnS_3 which acts as a flux during sintering. A density of

97% of theoretical was obtained with a mean grain size of about 30 μm at 1000°C. In both cases, however, additives served as activators to improve electroluminescent efficiency and were not acceptable for optical applications.

High vapor pressure of ZnS at elevated temperatures, on the other hand, is utilized to grow flat polycrystalline parts by chemical vapor deposition (CVD). In spite of the good deposition efficiency, CVD grown ZnS exhibits cubic and hexagonal phases which cause significant scattering losses [3]. Another setback of the CVD technique is the inability to control grain size. For example, CVD grown ZnS parts usually show an average grain size of about 15 μm [4]. A detailed discussion of the preparation and properties of CVD grown ZnS is given by Savage [5].

Hot pressing and hot isostatic pressing provide unique means for preparing materials with higher densities and smaller grain sizes than can be achieved by pressureless sintering or by CVD, especially for nonoxides. Transluscent ZnS has been prepared by hot pressing in molybdenum dies at 800-870°C and 25 MPa for 15 minutes [6]. However, no information was given about the microstructure of the pressed parts. Carnall [7] has also prepared >99.9% dense, optically-transparent ZnS pieces by hot pressing at 750°C and 290 MPa in Mo-alloy dies. The mean grain size was around 10-15 μm and etched surfaces showed extensive twinning.

Densification of a compact during hot pressing proceeds through several mechanisms, including particle fracture and rearrangement,

plastic flow, lattice and grain boundary diffusion, and power-law creep. When a pressure is applied to a powder compact, particle rearrangement takes place, bringing the relative density up to about 60% of theoretical. The process is time and temperature independent, at least in the range investigated, and is believed to be a multistage process; translational restacking is followed by sliding until particles lock in due to neck formation and plastic deformation. Applied pressure is transmitted through the compact as a set of forces acting through the particle contacts. Effective pressures higher than the yield strength of the material cause plastic deformation which increases contact areas until they can support the forces without further yielding. Temperature-dependent plastic flow begins immediately with the application of pressure (and simultaneously with particle fracture and sliding), so that densification by other time-dependent processes begins following plastic flow. The starting density for these processes is given by [8]:

$$\rho_y = \left(\frac{(1-\rho_o)P}{1.3\ \sigma_y} + \rho_o^{\,3} \right)^{1/3} \qquad (1)$$

during initial stage (D < 90%) and,

$$\rho_y = 1 - \exp\left(-\frac{3}{2} \frac{P}{\sigma_y} \right) \qquad (2)$$

during final stage (D > 90%), where ρ_o is initial relative density of the green compact, P is the applied pressure and σ_y is the yield

strength of the material at that temperature.

Two important time-dependent densification mechanisms are power-law creep and grain boundary diffusion. The former governs the deformation at the particle contacts, while the latter relates to atomic diffusion at these boundaries which results in material transport from boundaries to fill up the neck areas much like in pressureless sintering. When the grain size is significantly smaller than the starting particle size, another mechanism, Nabarro-Herring and Coble creep (diffusion flow), becomes another important contributor to densification. In addition to these mechanisms, twinning may contribute to densification as well.

All of these processes enlarge the contact area and the number of contacts between particles so that the effective pressure decreases. This can change the dominant mechanism, which depends not only on the external variables (i.e., applied pressure and temperature), but also on the internal parameters of the compact, such as relative density, interparticle neck size and instantaneous grain geometry. It may, therefore, be expected that the contribution of each mechanism will change with time. Furthermore, the overall behavior is complicated because each mechanism has a different dependence on particle size, temperature, pressure and grain geometry.

Models and rate expression for these mechanisms have been thoroughly studied and are presented in Table 1.. These expressions consist of approximations as discussed in detail by Helle et al. [8]. Application of these expressions to the analysis of a given system

Table 1. Rate expressions for various densification mechanisms assuming they operate independently

	Initial stage ($\rho < 0.9$)	Final stage ($\rho > 0.9$)
Power-law creep	$5.3(\rho^2\rho_o)^{1/3}\,\frac{X\cdot C}{R}\left(\frac{P_{eff}}{3}\right)^n$	$\frac{3C}{2}\,\frac{(1-\rho)}{(1-(1-\rho)^{1/n})^n}\left(\frac{3}{2n}P\right)^n$
Boundary diffusion	$\frac{(1-\rho_o)^2}{(\rho-\rho_o)^2}\cdot C'\cdot\Omega\cdot P$	$C'''\cdot\Omega\cdot(1-\rho)^{1/2}\cdot P$
Nabarro-Herring and Coble creep	$24.9\,(\rho^2\rho_o)^{1/3}\,\frac{X\cdot C''\cdot\Omega}{RkTG^2}\,P_{eff}$	$31.5\,\frac{\Omega\cdot(1-\rho)}{kTG^2}\cdot C''\cdot P$

$$C = \frac{AbD_v}{kT\mu^{n-1}} \qquad C''' = \frac{270\,(\delta D_b + rD_v)}{kTR^3}$$

$$C' = \frac{43(\delta D_b + \gamma D_v)}{kTR^3} \qquad X = \frac{R}{\sqrt{3}}\left(\frac{\rho-\rho_o}{1-\rho_o}\right)^{1/2}$$

$$C'' = D_v + \frac{\pi\delta D_b}{G} \qquad r = R\left(\frac{1-\rho}{6}\right)^{1/3}$$

Table 1. Continued

Initial stage ($\rho < 0.9$)	Final stage ($\rho > 0.9$)
$\gamma = R\ (\rho-\rho_o)$	$P_{eff} = \frac{P(1-\rho_o)}{\rho^2(\rho-\rho_o)}$

requires careful control over particle properties and a priori knowledge of a number of material parameters including strength, modulus and diffusion constants as a function of temperature. Several researchers [8-13] have used the expressions given in Table 1 to develop densification maps for various materials. The maps are constructed by evaluating the rate equations at sets of values of ρ vs. P, ρ vs. T, or P vs. T. The dominant mechanism is identified as that which gives the greatest contribution to the densification. Field boundaries are determined by equating the rate expressions for relevant mechanisms.

The rate of densification is maximized when powders with uniform particles and high surface energy are employed. Preparation of high purity ZnS powders with spherical, submicron size particles has been reported previously [14-15]. The primary purpose of this work was to investigate the densification behavior and development of microstructure of these monodisperse, submicron size particle assemblies. The influence of time, temperature, and applied pressure on the final density and on the average grain size was investigated. An attempt was made to determine the relative contribution of various mechanisms to densification at various stages of the process.

EXPERIMENTAL

ZnS powders with spherical, submicron size particles were homogeneously precipitated from acidic zinc solutions by thermal decomposition of thioacetamide; a complete description of the procedure is given elsewhere [14, 15]. X-ray diffraction patterns of the as-prepared powders revealed only the β-ZnS (sphalerite) phase. The spherical particles used in this study were quite uniform with a mean diameter of 0.35 μm.

Powders were sieved through a 200-mesh nylon screen to break large agglomerates which might cause nonuniform green microstructure. Pellets were formed by dry pressing uniaxially about 0.40 grams of powder to 3.50 MPa in a 0.95 cm diameter double-acting steel die. The pellets were further compacted to 200 MPa isostatically. Densities of the green pellets were determined from geometric measurements. The pore entry size distribution of a representative pellet was determined by mercury porosimetry.

A controlled atmosphere/vacuum hot press (Astro HP-22-0614SC) equipped with a Honeywell DCP 770011 controller and a manually controlled, motor-driven hydraulic pump was employed. Applied pressure and ram travel (deformation) were monitored on digital panel meters and recorded continuously. Preset gas flow rates were programmed as a function of temperature and/or time and changed during the experiments automatically through the controller. Hot-pressing experiments were conducted using fine-grained graphite dies under flowing nitrogen

atmosphere with various combinations of times, temperatures and pressures, in the range of 1 to 120 minutes, 750 to 900°C at 50°C intervals, and 7.5 MPa to 175 MPa. Isostatically pressed pellets were loaded into the graphite assembly and were initially heated at 250°C for 20 minutes with a nitrogen gas flow rate of 10 lt. min^{-1}, to help remove any adsorbed gases and purge the system. The nitrogen gas flow rate was reduced to 5 lt. min^{-1} at the end of the initial heating period and the temperature was increased at such a rate to reach the prescribed peak temperature in one hour. The pressure was applied six minutes after peak temperature was reached to allow stabilization of temperature. Applied pressure and temperature were controlled as close as $\pm$ 0.5 MPa and $\pm$ 5°C, respectively. Pressure was released after a predetermined period, and the specimen was cooled to room temperature. The time elapsed between pressure application and release was taken as the hot-pressing time.

After ejection from the die, a thin layer of graphite contamination was ground away and the bulk densities of the hot-pressed specimens were measured by liquid immersion techniques. Distilled water was used as the immersion liquid. A value of 4.10 $g \cdot cm^{-3}$ was taken as the theoretical density for β-ZnS [16]. Sectioned and polished specimens were chemically etched with 10 M hydrochloric acid at 80°C, and the development of microstructure was examined by SEM. Fracture surfaces of a number of pellets were also studied in order to assess the fracture mode at various stages of densification.

RESULTS AND DISCUSSION

Green Compact

Pore entry size distribution for a representative green pellet is given in Figure 1. A narrow distribution of pore entry sizes ranging between 20 and 50 nm with a maximum at 35 nm was observed. A calculated pore entry radius for monosized particles of 0.35 μm diameter yields 25 nm for 3-point contacts and 70 nm for 4-point contacts. Comparison of pore entry size distribution in Figure 1 with calculated pore radii implies that the powder packing is random with a combination of coordination numbers of 6 (4-point contacts) and 8 or 12 (3-point contacts). The coordination number of a compact is related to the relative density, ρ, by

$$Z = 12 \cdot \rho \tag{3}$$

which approaches 12 at full density and 7 at a relative density of 60% (corresponding to random packing). The relative densities of the isostatically pressed pellets were around 45% as determined by geometric measurements. The total pore volume obtained from mercury porosimetry corresponded to a relative density of 52%. The slightly higher value of relative density obtained from mercury porosimetry is probably a consequence of further compaction of the pellets due to applied pressures twice (400 MPa) as high as the isostatic pressing pressure. The discrepancy between measured and calculated (from Eq. 3)

Figure 1. Pore entry size distribution of a typical pellet prior to hot pressing. Pellet was dry pressed at 7 MPa followed by cold isostatic pressing at 200 MPa

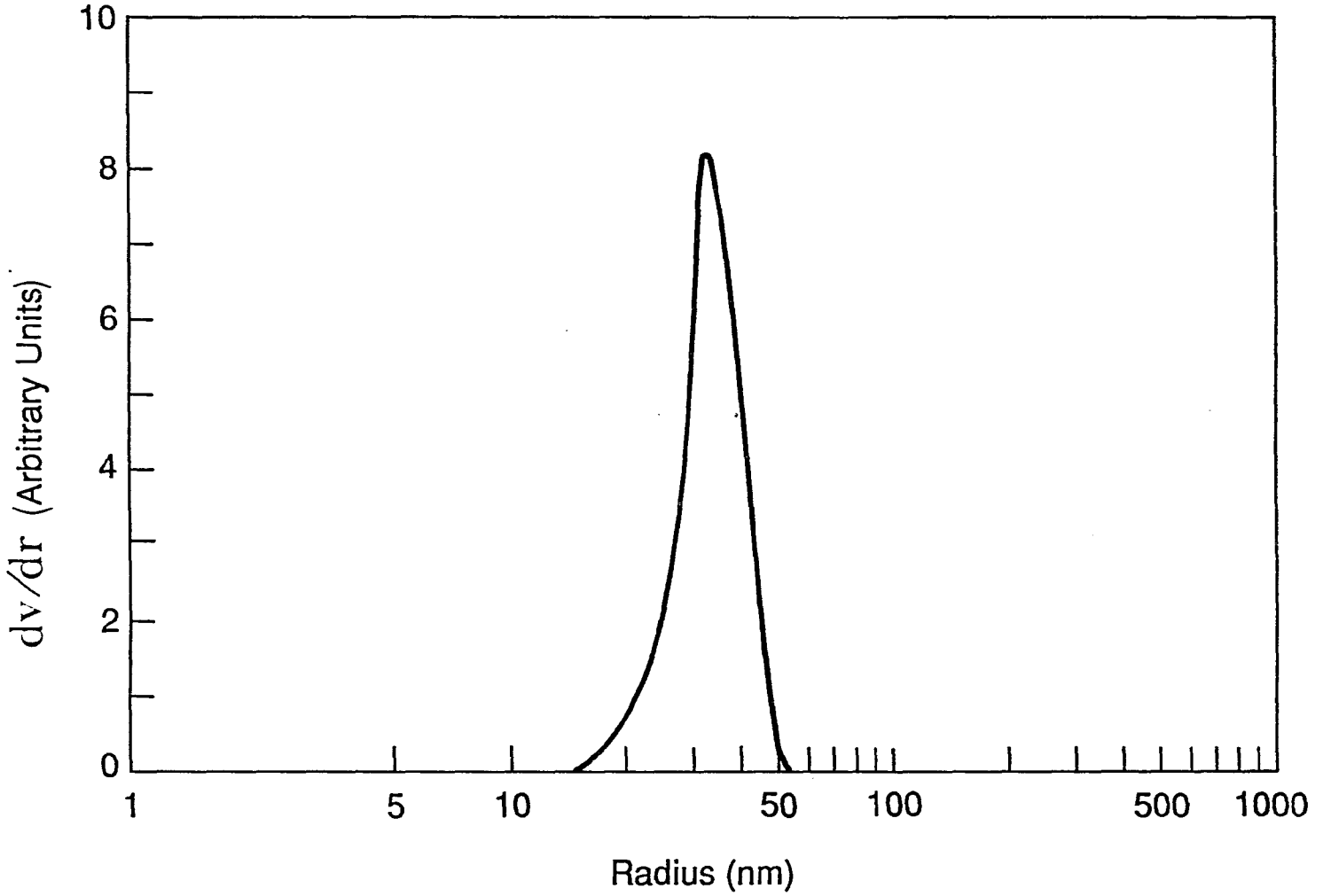
10
8
6
4
2
0
dv/dr (Arbitrary Units)
1
5
10
50
100
500
1000
Radius (nm)

is obviously due to inhomogeneous packing. Another reason for lower densities than those expected from a random packing is due to the fact that the individual particles were porous agglomerates of about 15 nm crystallites [14]. The pore entry radius of intraparticle pores, however, is too small ($\leq$ 1.00 nm) to be detected by mercury porosimetry. A scanning electron micrograph of a green pellet is given in Figure 2. The micrograph indicates that particle packing is random, but not dense. Voids as large as several particle diameters are observable. Obviously, mercury porosimetry does not reveal any information about the pore bodies, but rather gives the constricted pore-neck size. Nevertheless, the contribution of these multiparticle size pores to total porosity of the green compact is less than that from the interstitial porosity.

Densification

The influence of hot-pressing time, temperature and pressure on densification and grain growth processes was studied by determining the final density and by scanning electron microscopic observations of both fractured and polished-etched surfaces. Table 2 and Figures 3-5 show the variation of relative density of hot-pressed compacts as a function of time at 800, 850 and 900°C, respectively, for various pressures employed. Although not shown on the graphs, the initial densities at zero time at corresponding temperatures were determined on pellets that were heated to peak temperature and soaked for six minutes. These "pressureless sintering" density values for different

Figure 2. Scanning electron micrograph of fracture surface of a representative green pellet

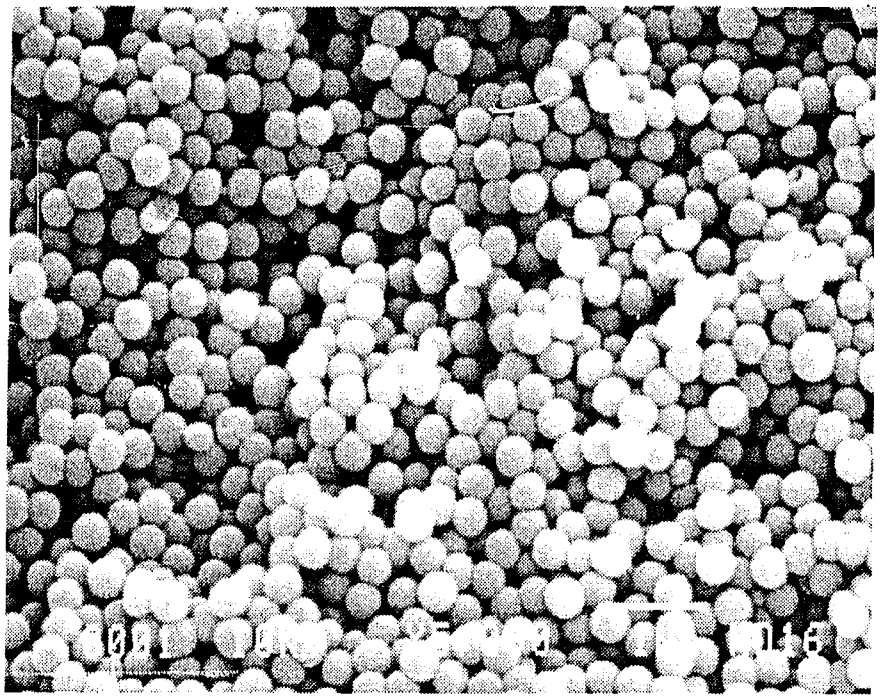

Table 2. Percent relative densities of ZnS compacts at various times for given hot-pressing temperatures and pressures

Temperature (°C)	Time (min)	P=17.5MPa	P=35MPa	P=70MPa	P=105MPa
800	1	77.83	85.95	--	95.15
800	3	83.47	91.61	--	97.28
800	6	85.01	92.86	--	98.24
800	12	86.53	93.36	--	98.62
800	18	90.60	94.56	--	97.98
800	24	91.81	94.72	--	97.98
800	30	92.52	96.11	--	98.09
800	60	92.60	96.80	--	--
850	1	80.23	87.25	--	97.17
850	3	82.63	88.47	--	97.98
850	6	85.96	91.73	--	98.39
850	12	90.58	94.28	--	98.45
850	18	93.01	96.25	--	99.07
850	24	94.52	96.89	--	98.98
850	30	94.96	97.59	--	98.71
850	60	95.41	97.89	--	--
900	1	87.73	94.31	96.33	97.27
900	3	92.14	95.49	96.25	98.49
900	6	93.00	95.88	97.58	99.10
900	12	93.58	96.08	98.63	99.54
900	18	93.91	97.08	98.70	99.57
900	24	94.92	97.49	98.70	99.73
900	30	95.67	97.71	98.78	99.51
900	60	--	97.79	99.10	99.49

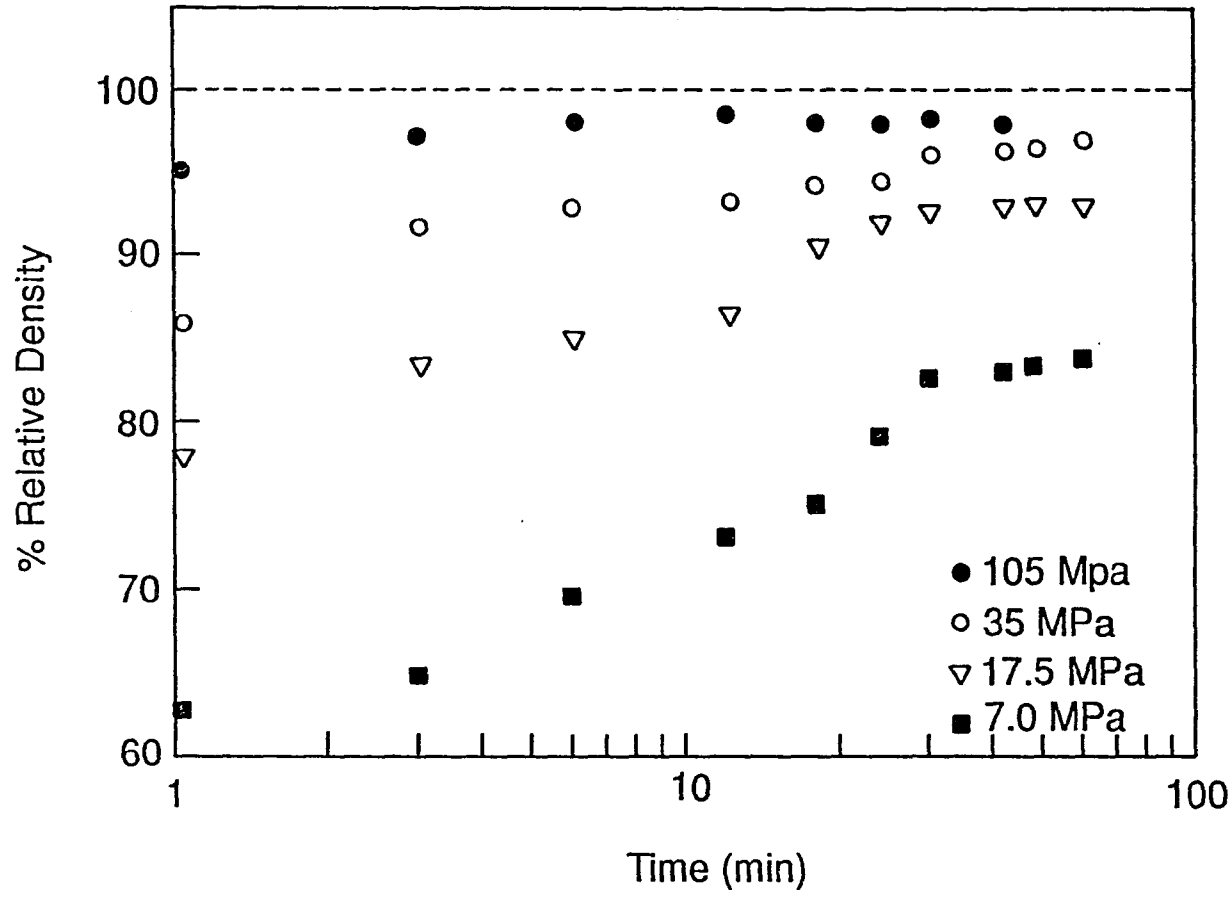

Figure 3. Variation of percent relative density with time at 800°C at various pressures

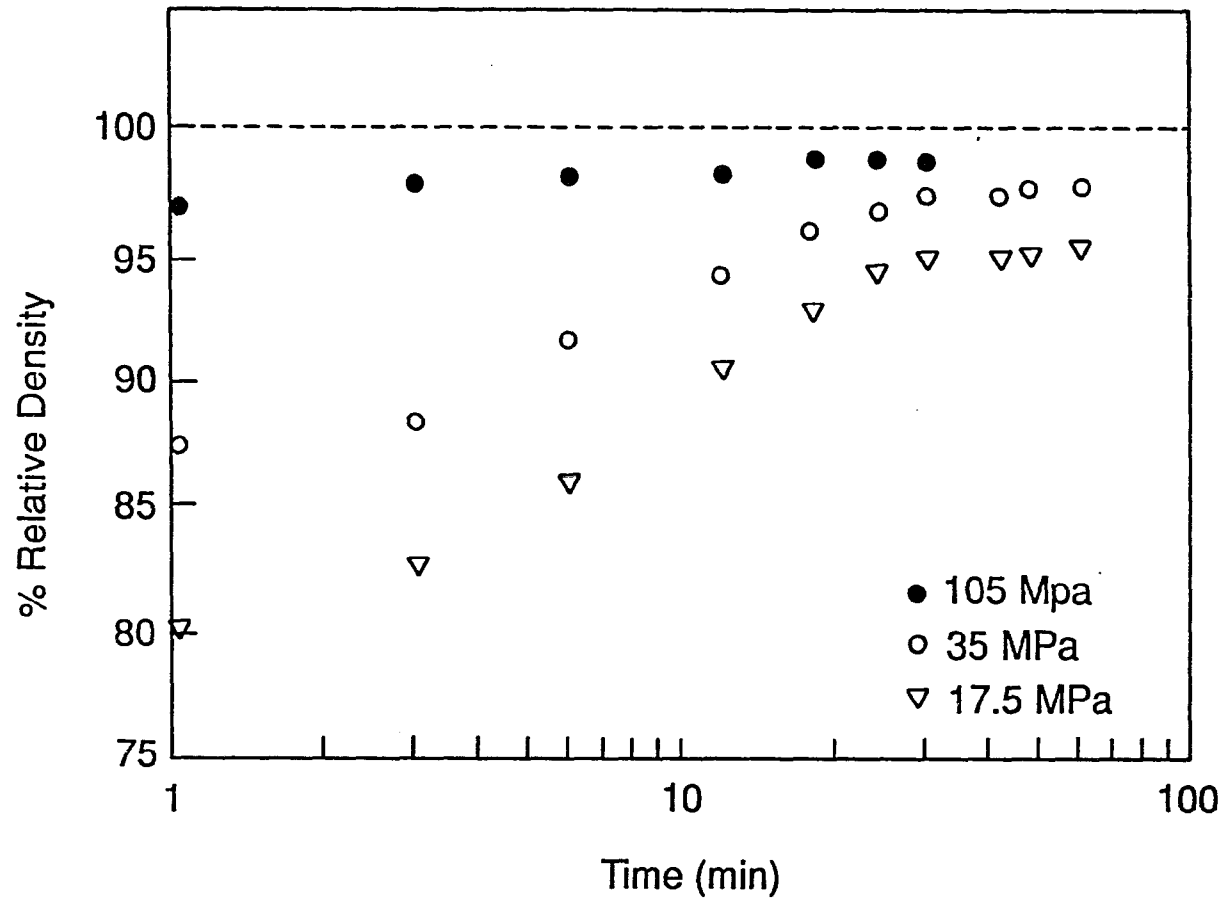

Figure 4. Variation of percent relative density with time at 850°C at various pressures

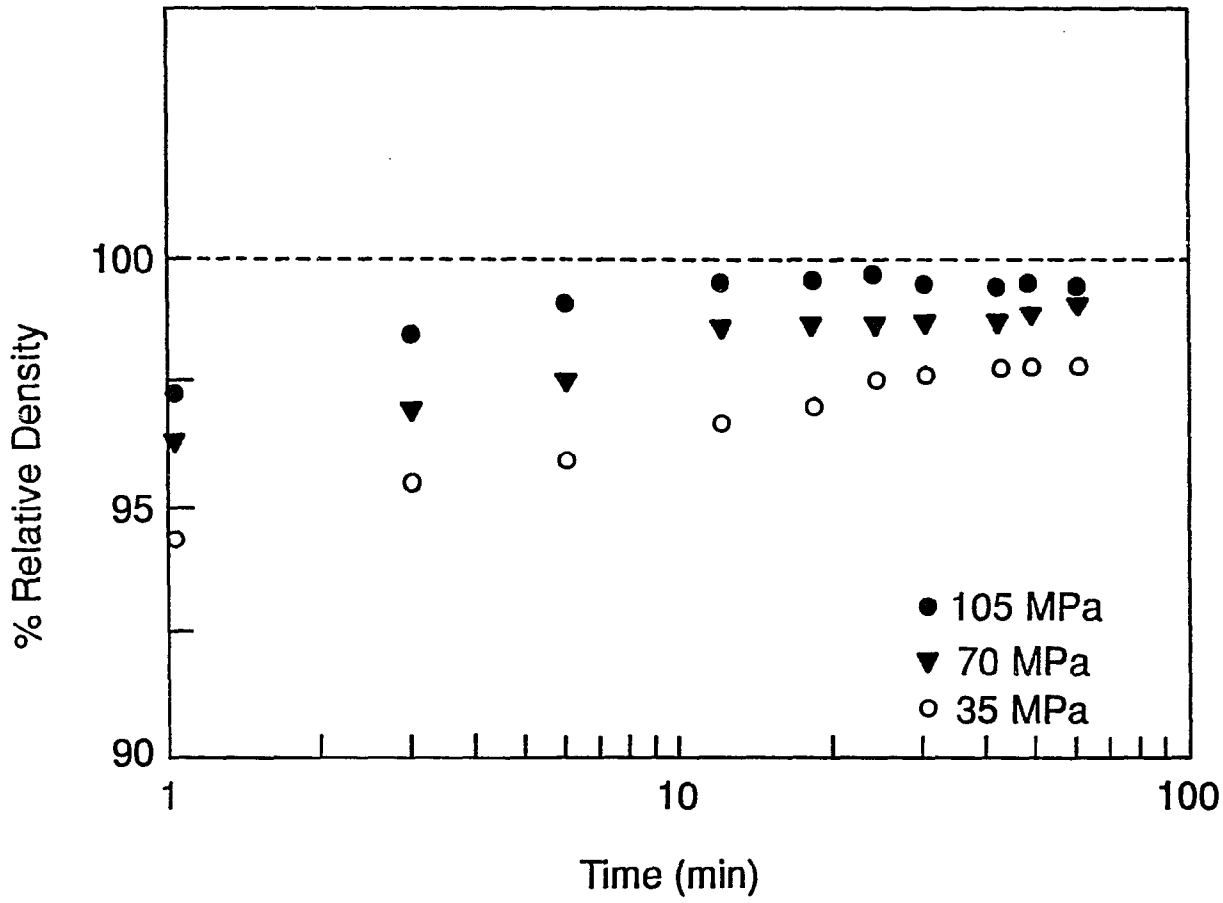

Figure 5. Variation of percent relative density with time at 900°C at various pressures

peak temperatures remained more or less constant around 55%. During hot pressing, increasing time, temperature and pressure resulted in higher final densities. Comparison of the densities after one minute of pressing indicates that only slight densification occurred at low pressure and temperature, while better than 96% density was achieved at higher pressures and temperatures. Near theoretical densities (>99%) were obtained in six and 15 minutes at 900 and 850°C, respectively, for pressing at 105 MPa. It is important to note that although densities greater than 99% theoretical had been achieved previously [6, 7], the pressures applied in those studies were much higher than in the present study. It is the opinion of the authors that fine and uniform particle assemblies afford attainment of high densities at moderate pressure, temperature and time conditions.

Maximum achievable (final) densities for any given set of hot-pressing conditions were reached in a maximum of 30 minutes, as indicated by low rates of change of relative density beyond this time. Beyond 30 minutes, the densification process is believed to approximate normal sintering. A slight decrease in relative densities of compacts hot pressed at 105 MPa was observed beyond 24 minutes. This reduction in relative density is believed to result from nucleation of intergranular pores. Similar behavior was observed by Xue and Raj [17] on hot-pressed ZnS specimens deformed at high rates at temperatures around 1000°C.

An important feature of the relative density versus log time curves is that they exhibit a S shape with a steep inflection point at

low pressures and temperatures. The steepness of the inflection point is lessened and its location is shifted to shorter times with increasing applied pressure. Eventually, the shape of the relative density-log time curves becomes essentially flat at the highest pressures. A similar trend is observed with increasing temperature, especially at lower applied pressures. This gradual change in the response of the powder toward experimental variables suggests that several densification mechanisms may be operative. The contribution of each mechanism to the densification process appears to vary with the process variables and instantaneous relative density.

Microstructure Evolution

A matrix of scanning electron fractographs of specimens hot pressed for 30 minutes at various temperatures and applied pressures is given in Figure 6. The variation of grain size with temperature and pressure is plotted in Figures 7(a) and (b), respectively. For purposes of direct comparison, the hot-pressing time was kept constant at 30 minutes for all combinations of temperature and pressure. An examination of Figure 6 and the data presented in Figures 7(a) and 7(b) shows that increasing pressure up to 35 MPa at a given temperature increases the grain size. At still higher applied pressures, smaller grains are observed. This is perhaps due to particle fragmentation at high pressures. A slight increase in grain size with increasing temperature is observed for any given applied pressure. Nevertheless, in all of the experiments, the grain size remained less than 1.3 μm.

Figure 6. Scanning electron fractographs of hot pressed specimens at indicated temperatures and pressures for 30 minutes

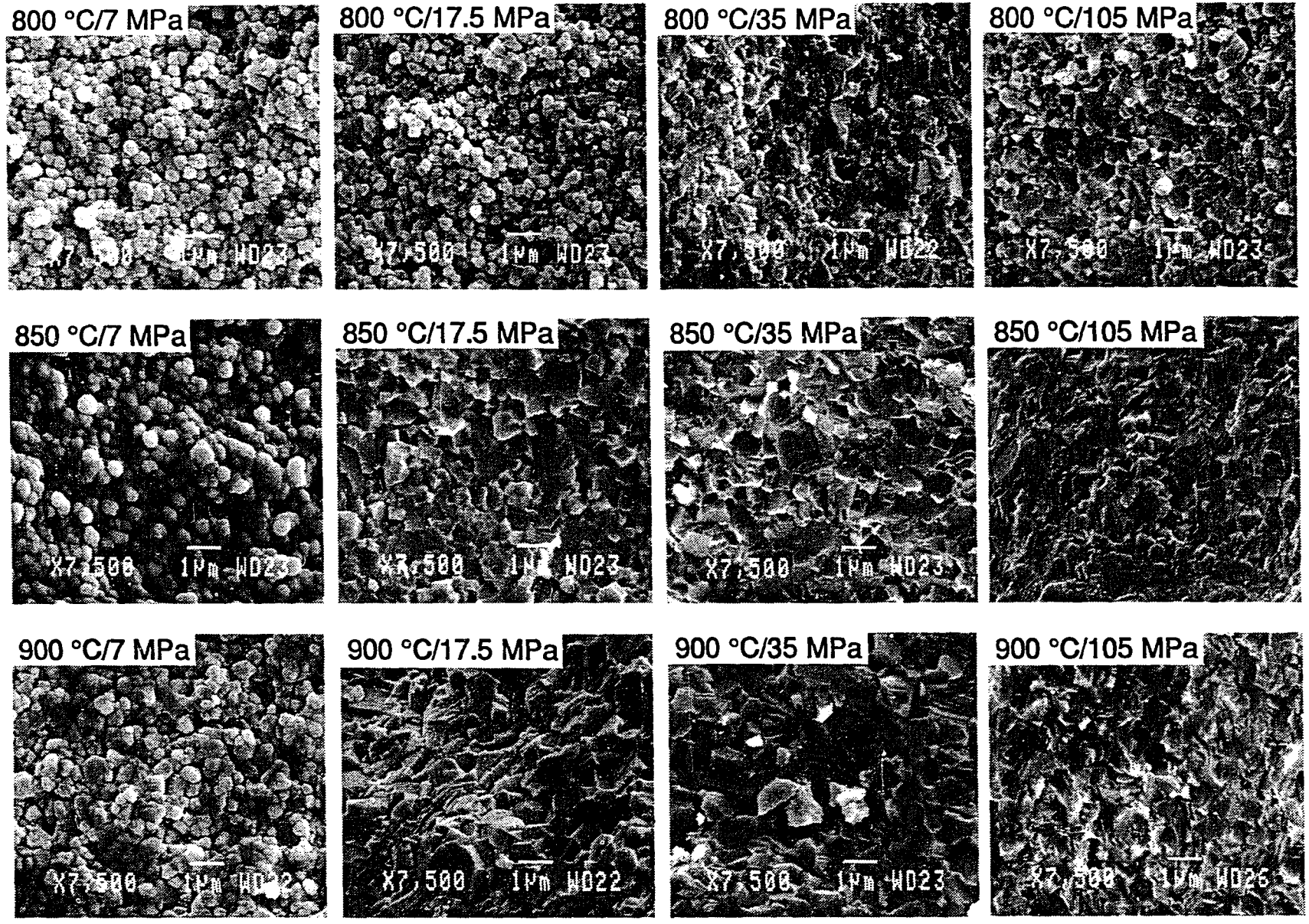
800 °C/7 MPa
800 °C/17.5 MPa
800 °C/35 MPa
800 °C/105 MPa
850 °C/7 MPa
850 °C/17.5 MPa
850 °C/35 MPa
850 °C/105 MPa
900 °C/7 MPa
900 °C/17.5 MPa
900 °C/35 MPa
900 °C/105 MPa

Figure 7. Variation of grain size a) with pressure at various temperatures and b) with temperature at various pressures

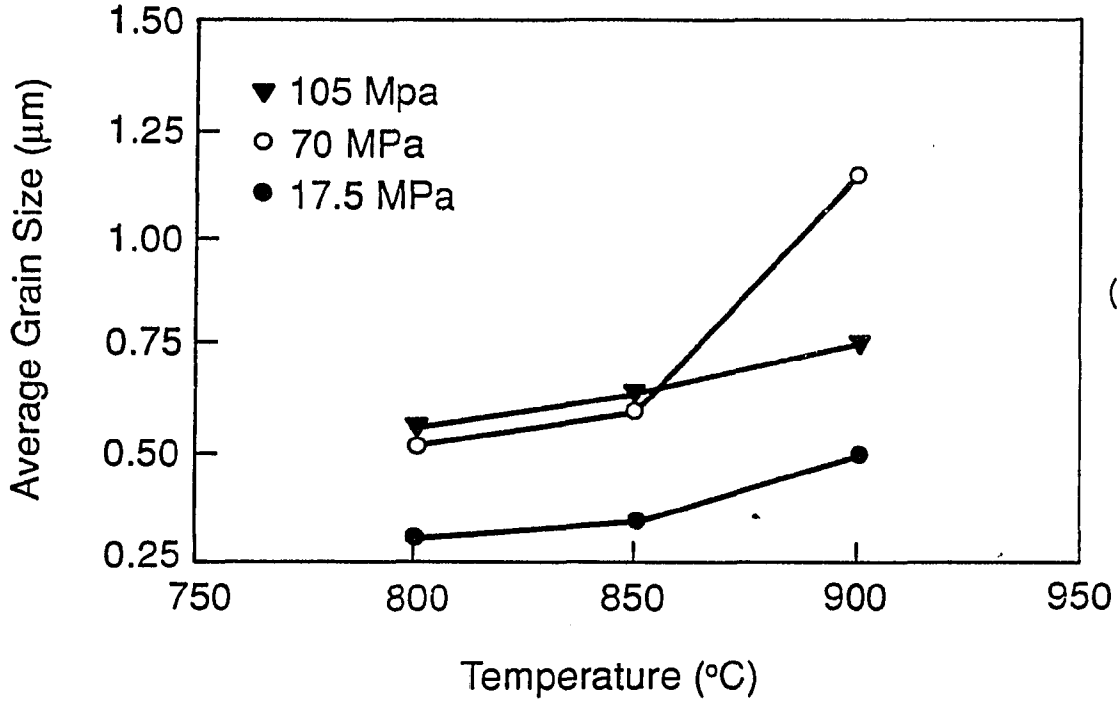
1.50
1.25
1.00
0.75
0.50
0.25
Average Grain Size (μm)
▼ 105 Mpa
○ 70 MPa
● 17.5 MPa
750
800
850
900
950
Temperature (°C)

(a)

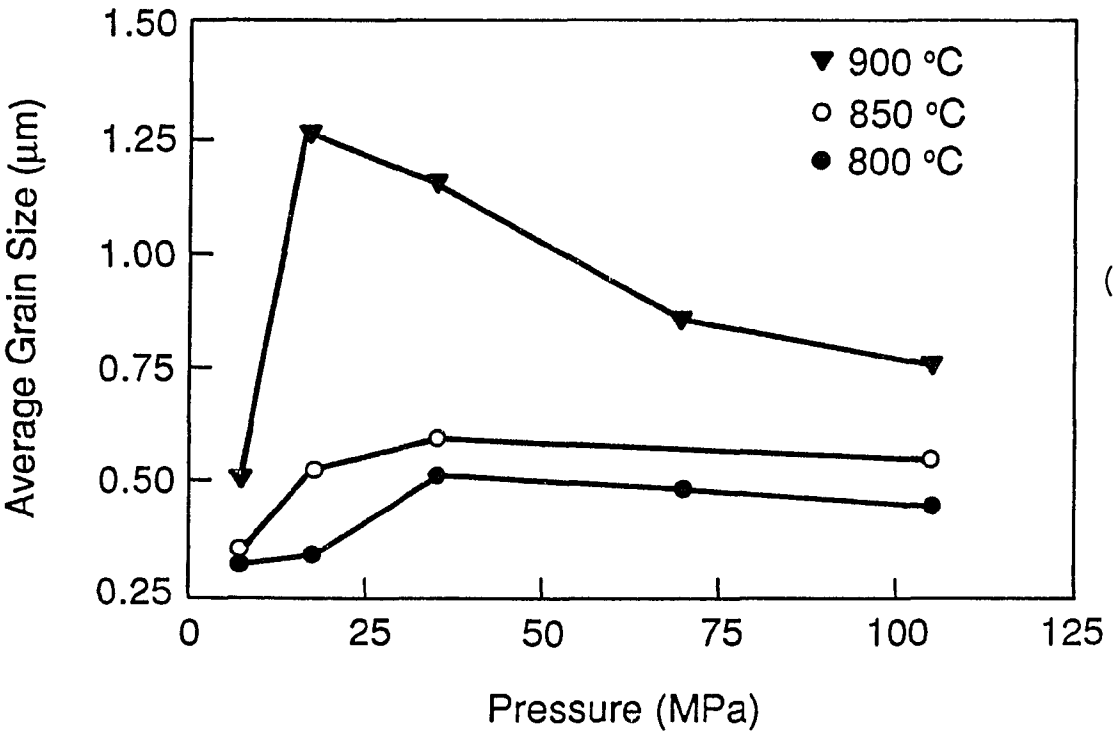
1.50
1.25
1.00
0.75
0.50
0.25
Average Grain Size (μm)
▼ 900 °C
○ 850 °C
● 800 °C
0
25
50
75
100
125
Pressure (MPa)

(b)

The qualitative examination of the fractographs in Figure 6 also reveals that the mechanism of fracture gradually changes from intergranular to transgranular as the applied pressure and temperature increased. These observations suggest that intergranular diffusion becomes significant at the higher pressures and temperatures, and that the strengthening of grain boundaries is diffusion controlled.

Figures 8-10 show the development of microstructure at 800°C and 17.5 MPa, 800°C and 105 MPa, and 900°C and 17.5 MPa, respectively. Comparison of Figures 8 and 9 shows the influence of applied pressure, while that of Figures 8 and 10 shows the influence of temperature on the densification. Figure 8(a) is the polished-etched surface of a compact after three minutes of hot pressing. Micrographs clearly display the distinct features of initial stage densification ($D < 90\%$). Original particles are still discernible, but significant neck growth has already occurred. The pores are uniformly distributed and interconnected. The average grain size, at this stage, is slightly less than the starting particle size (0.35 μm), probably due to the fracture of particles by applied pressure. Another reason for observing smaller grain sizes than the starting particle size may be attributed to the polycrystallinity of the starting particles. Upon application of temperature and pressure, these polycrystalline particles may fuse together which results in particles smaller than the original size. In Figure 8(b) (12 minutes), it appears that the pore phase is less interconnected, but no significant grain growth is observed. Pores continue to be eliminated as the densification

Figure 8. Development of microstructure at 800°C and 17.5 MPa after a) 3 min., b) 123 min., c) 18 min., and d) 30 min. of pressure application

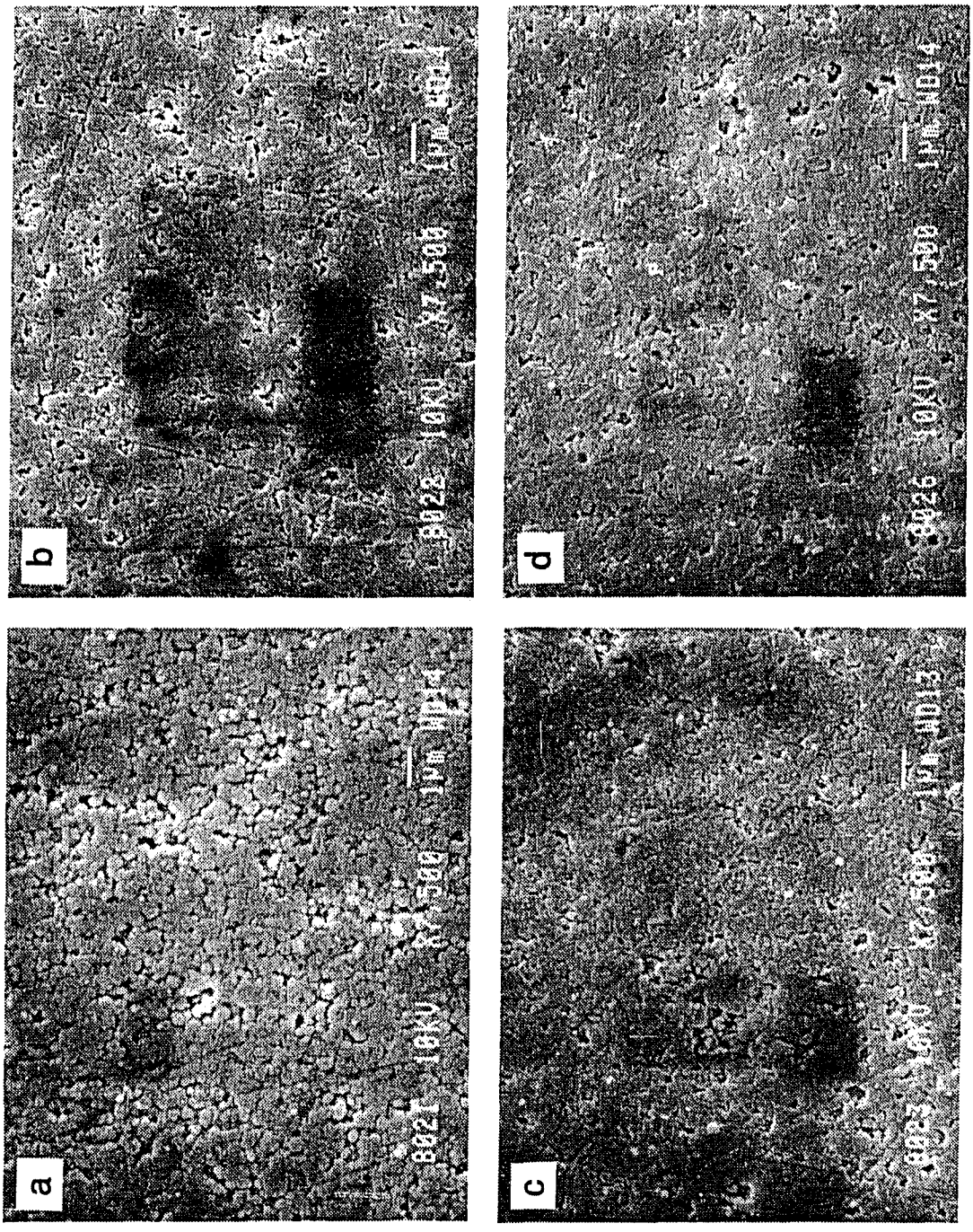
a
b
c
d

Figure 9. Development of microstructure at 80°C and 105 MPa after a) 3 min., b) 12 min., c) 18 min., and d) 30 min. of pressure application

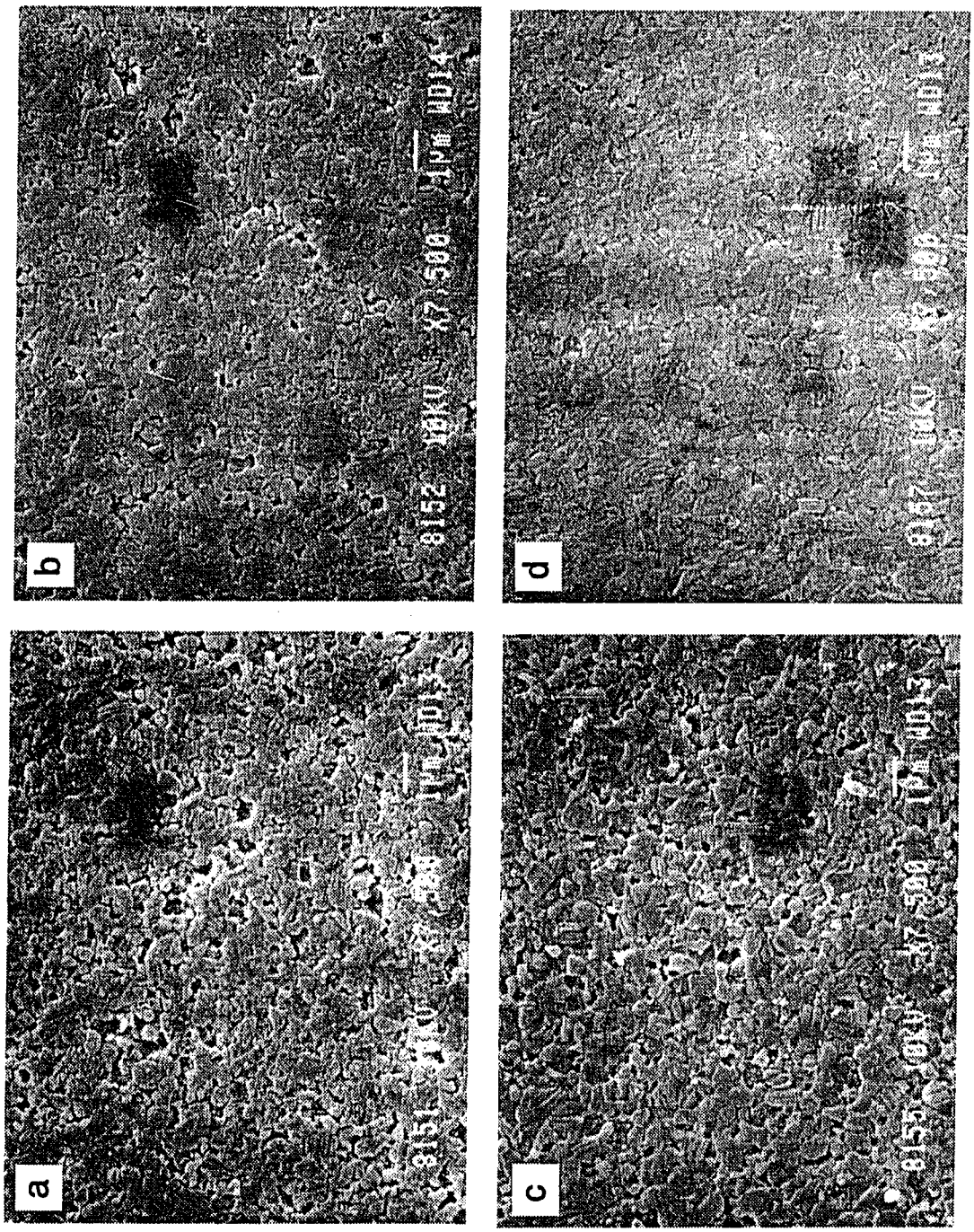
a
b
c
d

Figure 10. Development of microstructure at 900°C and 17.5 MPa after a) 3 min., b) 12 min., c) 18 min., and d) 30 min. of pressure application

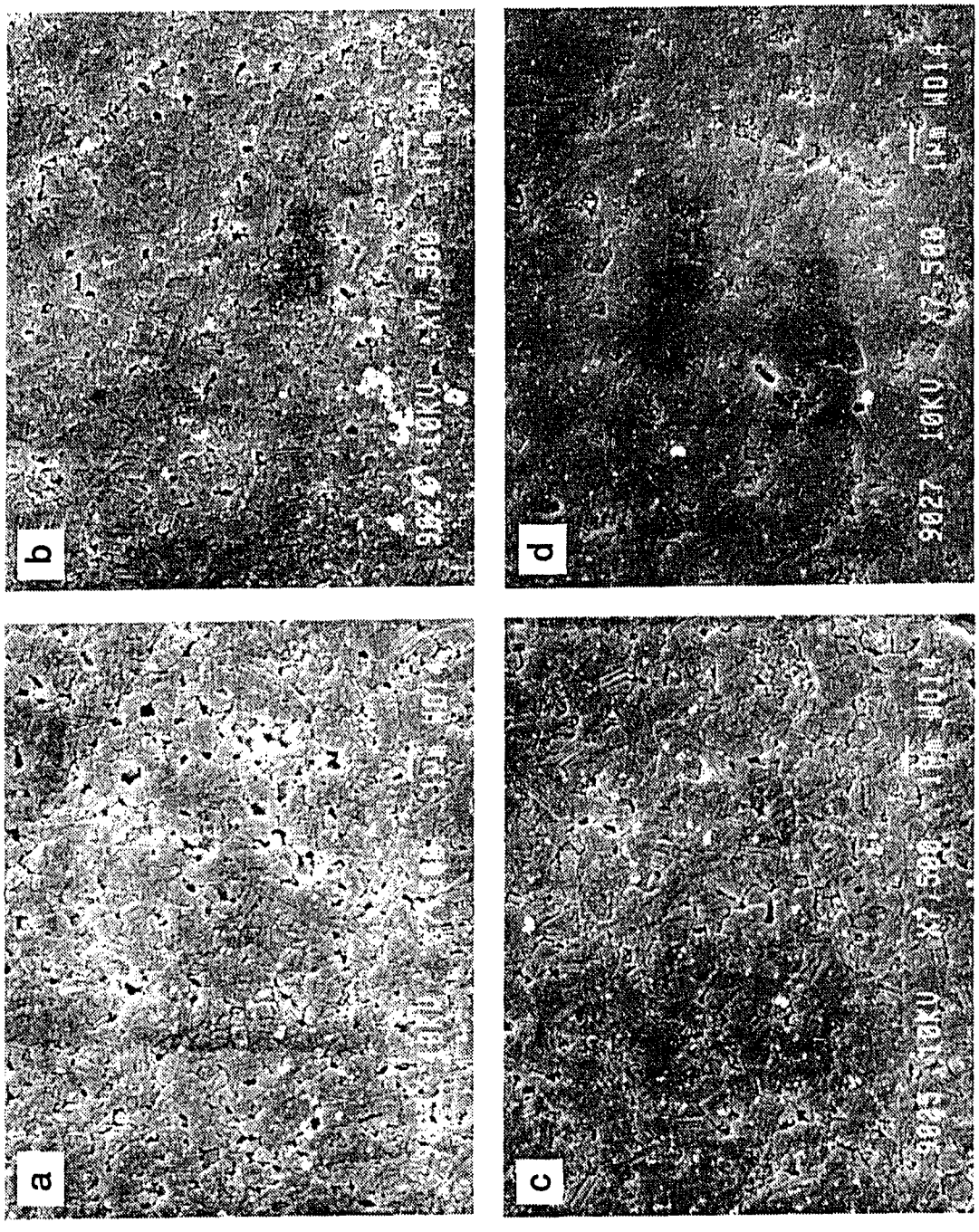
a
b
c
d

progresses (Figure 9(c)). Finally, pores become more or less isolated at 30 minutes of hot pressing. However, grain pull-outs during polishing are inevitable and must be distinguished from true pores.

Comparison of Figure 8 with Figures 9 and 10 reveals accelerated densification kinetics as hot-pressing temperature and applied pressure were increased. For example, the compact reaches the final stages at 800°C and 105 MPa in 12 minutes, while it requires only three minutes at 900°C and 17.5 MPa, as seen in Figures 9(b) and 10(a). Both pore volume and pore size are smaller at higher temperatures and/or pressures at comparable times (Figures 9(b), 9(c), 10(b) and 10(c)). An almost pore-free state had been reached in 30 minutes (Figures 9(d) and 10(d)) for these conditions.

Densification Mechanisms

A number of material properties used to plot densification maps and determine the dominant densification mechanisms operative in hot-pressing experiments as described in the previous sections are given in Table 3. The diffusion coefficients are considered to be the least reliable of all. We have used a pre-exponential factor and an activation energy value that were obtained under a sulfur pressure of 0.5 atm [18]. However, the defect concentration of a compound, and thus the diffusion coefficient, changes significantly with atmosphere. We performed the hot-pressing experiments under a flowing nitrogen atmosphere, so that the actual diffusion coefficients might be higher than those given in Table 3. The value of the stress exponent was

Table 3. Material properties for ZnS

Atomic volume, Ω (m^3)	3.96×10^{-29}
Burger's vector, b (m)	2.70×10^{-10}[a]
Melting temperature, Tm (°K)	2103
Yield strength, σ_y (MPa)	60[b]
Shear modulus, M (MPa)	2.9×10^{3}
Volume diffusion coeff., D_v (m^2/sec)	3.53×10^{-7} exp (-235000/RT)
Boundary diffusion coeff., D_b (m^2/sec)	3.05×10^{-7} exp (-210000/RT)[c]
Boundary thickness, δ (m)	10×10^{-10}[d]
Stress exponent, n	5
Dorn constant, A	3.26×10^{6}

[a]Data for the slip system - {111} <110> [19].

[b]Data given in the table are at 900°C and at a strain rate of 1.5×10^{-5} sec^{-1}, which is similar to those observed in our experiments.

[c]Determined by comparison with similar structured materials having comparable melting temperature.

[d]Estimated value assuming several atomic layers.

taken as five by comparing ZnS with materials having similar structure and comparable melting points. The Dorn constant, A, was estimated from a relation given in [20]:

$$\log A = -10.5 + 3.4\, n \quad . \tag{4}$$

Yield strengths of 60, 120 and 180 MPa were taken from the data of Xue and Raj [17] for temperatures of 900, 850 and 800°C, respectively, and at a strain rate of 1.5×10^{-5} sec^{-1}.

Tables 4-6 are the estimated densification rates by individual mechanisms at varying relative densities under given combinations of temperature and applied pressure assuming that they operate independently. For every combination of external variables, relative density was varied from the value reached by plastic flow (calculated from Eqs. 2 and 3) to full density at which the densification rate equals zero. It is obvious that Nabarro-Herring and Coble creep (diffusional flow) never becomes dominant within the range of temperatures and pressures studied. This mechanism is believed to be dominant when the average grain size is less than our initial particle size. In our calculations, we have used a constant average grain size of 0.5 μm. Indeed, the average grain size varied with time and in some cases, was smaller than the initial particle size (see Figure 8(a)). For this reason, the contribution of Nabarro-Herring and Coble creep is expected to be higher than given in these tables, especially at the initial stages of the process (at low temperatures).

Table 4a. Variation of densification rate by individual mechanisms with relative density at 800°C and 17.5 MPa

Relative density	Boundary diffusion ($\times 10^4$ sec^{-1})	Nabarro-Herring and Coble creep ($\times 10^4$ sec^{-1})	Power-law creep ($\times 10^4$ sec^{-1})
0.600	2.778	0.131	2.901
0.625	2.216	0.112	0.727
0.650	1.761	0.097	0.222
0.675	1.480	0.085	0.078
0.700	1.273	0.076	0.031
0.725	1.115	0.068	0.013
0.750	0.991	0.062	0.006
0.775	0.891	0.057	0.003
0.800	0.809	0.052	0.001
0.825	0.741	0.048	0.000
0.850	0.683	0.044	--
0.875	0.633	0.041	--
0.900	0.454	0.038	--
0.925	0.336	0.006	--
0.950	0.203	0.004	--
9.975	0.152	0.002	--
1.000	0.000	0.000	--

Table 4b. Variation of densification rate by individual mechanisms with relative density at 800°C and 35 MPa

Relative density	Boundary diffusion ($\times 10^4$ sec^{-1})	Nabarro-Herring and Coble creep ($\times 10^4$ sec^{-1})	Power-law creep ($\times 10^4$ sec^{-1})
0.625	5.556	0.223	23.260
0.650	4.326	0.193	7.102
0.675	3.522	0.170	2.495
0.700	2.959	0.152	0.974
0.725	2.546	0.137	0.413
0.750	2.230	0.124	0.187
0.775	1.983	0.113	0.090
0.800	1.783	0.103	0.045
0.825	1.619	0.096	0.024
0.850	1.482	0.089	0.013
0.875	1.365	0.082	0.007
0.900	1.266	0.077	0.004
0.925	0.908	0.012	0.001
0.950	0.672	0.008	0.000
0.975	0.405	0.004	0.000
1.000	0.000	0.000	0.000

Table 4c. Variation of densification rate by individual mechanisms with relative density at 800°C and 70 MPa

Relative density	Boundary diffusion ($\times 10^4$ sec^{-1})	Nabarro-Herring and Coble creep ($\times 10^4$ sec^{-1})	Power-law creep ($\times 10^4$ sec^{-1})
0.675	7.043	0.341	79.850
0.700	5.920	0.303	31.180
0.725	5.092	0.273	13.220
0.750	4.460	0.248	5.999
0.775	3.965	0.226	2.877
0.800	3.565	0.207	1.446
0.825	3.237	0.191	0.756
0.850	2.963	0.177	0.410
0.875	2.731	0.165	0.230
0.900	2.532	0.153	0.132
0.925	1.816	0.025	0.042
0.950	1.344	0.017	0.017
0.975	0.811	0.008	0.004
1.000	0.000	0.000	0.000

Table 4d. Variation of densification rate by individual mechanisms with relative density at 800°C and 105 MPa.

Relative density	Boundary diffusion ($\times 10^4$ sec^{-1})	Nabarro-Herring and Coble creep ($\times 10^4$ sec^{-1})	Power-law creep ($\times 10^4$ sec^{-1})
0.750	6.691	0.371	45.550
0.775	5.947	0.339	21.850
0.800	5.348	0.311	10.980
0.825	4.856	0.287	5.747
0.850	4.444	0.266	3.116
0.875	4.096	0.247	1.742
0.900	3.797	0.230	1.002
0.925	2.724	0.037	0.322
0.950	2.016	0.025	0.128
0.975	1.216	0.012	0.032
1.000	0.000	0.000	0.000

Table 5a. Variation of densification rate by individual mechanisms with relative density at 850°C and 17.5 MPa

Relative density	Boundary diffusion ($\times 10^4$ sec^{-1})	Nabarro-Herring and Coble creep ($\times 10^4$ sec^{-1})	Power-law creep ($\times 10^4$ sec^{-1})
0.600	11.160	0.403	8.968
0.625	8.179	0.341	2.244
0.650	6.402	0.296	0.685
0.675	5.234	0.260	0.241
0.700	4.413	0.231	0.094
0.725	3.808	0.209	0.040
0.750	3.344	0.189	0.018
0.775	2.978	0.173	0.009
0.800	2.683	0.159	0.004
0.825	2.440	0.146	0.002
0.850	2.236	0.135	0.001
0.875	2.064	0.126	--
0.900	1.915	0.117	--
0.925	1.359	0.019	--
0.950	1.002	0.013	--
0.975	0.060	0.006	--
1.000	0.000	0.000	--

Table 5b. Variation of densification rate by individual mechanisms with relative density at 850°C and 35 MPa

Relative density	Boundary diffusion ($\times 10^4$ sec^{-1})	Nabarro-Herring and Coble creep ($\times 10^4$ sec^{-1})	Power-law creep ($\times 10^4$ sec^{-1})
0.625	16.360	0.682	71.820
0.650	12.800	0.591	21.930
0.675	10.470	0.521	7.704
0.700	8.826	0.464	3.008
0.725	7.615	0.417	1.276
0.750	6.688	0.378	0.578
0.775	5.957	0.345	0.278
0.800	5.366	0.317	0.139
0.825	4.880	0.292	0.074
0.850	4.473	0.271	0.040
0.875	4.127	0.252	0.022
0.900	3.830	0.235	0.013
0.925	2.718	0.038	0.004
0.950	2.005	0.025	0.002
0.975	1.202	0.013	0.000
1.000	0.000	0.000	0.000

Table 5c. Variation of densification rate by individual mechanisms with relative density at 850°C and 70 MPa

Relative density	Boundary diffusion ($\times 10^4$ sec^{-1})	Nabarro-Herring and Coble creep ($\times 10^4$ sec^{-1})	Power-law creep ($\times 10^4$ sec^{-1})
0.725	15.230	0.835	40.830
0.750	13.380	0.757	18.520
0.775	11.910	0.691	8.882
0.800	10.730	0.634	4.464
0.825	9.759	0.584	2.337
0.850	8.945	0.541	1.267
0.875	8.254	0.503	0.708
0.900	7.661	0.469	0.408
0.925	5.436	0.076	0.131
0.950	4.010	0.050	0.052
0.975	2.404	0.025	0.013
1.000	0.000	0.000	0.000

Table 5d. Variation of densification rate by individual mechanisms with relative density at 850°C and 105 MPa

Relative density	Boundary diffusion ($\times 10^4$ sec^{-1})	Nabarro-Herring and Coble creep ($\times 10^4$ sec^{-1})	Power-law creep ($\times 10^4$ sec^{-1})
0.775	17.870	1.036	67.450
0.800	16.100	0.951	33.900
0.825	14.630	0.877	17.740
0.850	13.420	0.812	9.621
0.875	12.380	0.755	5.381
0.900	11.490	0.704	3.094
0.925	8.154	0.113	0.993
0.950	6.015	0.076	0.395
0.975	3.606	0.038	0.097
1.000	0.000	0.000	0.000

Table 6a. Variation of densification rate by individual mechanisms with relative density at 900°C and 17.5 MPa

Relative density	Boundary diffusion ($\times 10^4$ sec^{-1})	Nabarro-Herring and Coble creep ($\times 10^4$ sec^{-1})	Power-law creep ($\times 10^4$ sec^{-1})
0.625	21.990	0.948	6.282
0.650	17.290	0.821	1.918
0.675	14.190	0.723	0.674
0.700	12.000	0.644	0.263
0.725	10.380	0.594	0.112
0.750	9.135	0.525	0.051
0.775	8.150	0.480	0.024
0.800	7.354	0.440	0.012
0.825	6.696	0.406	0.064
0.850	6.145	0.376	0.035
0.875	5.676	0.349	0.019
0.900	5.273	0.326	0.011
0.925	3.707	0.052	0.004
0.950	2.727	0.035	0.001
0.975	1.626	0.018	0.000
1.000	0.000	0.000	0.000

Table 6b. Variation of densification rate by individual mechanisms with relative density at 900°C and 35 MPa

Relative density	Boundary diffusion ($\times 10^4$ sec^{-1})	Nabarro-Herring and Coble creep ($\times 10^4$ sec^{-1})	Power-law creep ($\times 10^4$ sec^{-1})
0.725	20.760	1.159	3.572
0.750	18.260	1.051	1.620
0.775	16.300	0.959	0.777
0.800	14.710	0.880	0.391
0.825	13.390	0.812	0.204
0.850	12.290	0.752	0.111
0.875	11.350	0.698	0.062
0.900	10.550	0.651	0.036
0.925	7.414	0.105	0.011
0.950	5.454	0.070	0.005
0.975	3.252	0.035	0.001
1.000	0.000	0.000	0.000

Table 6c. Variation of densification rate by individual mechanisms with relative density at 900°C and 70 MPa

Relative density	Boundary diffusion ($\times 10^4$ sec^{-1})	Nabarro-Herring and Coble creep ($\times 10^4$ sec^{-1})	Power-law creep ($\times 10^4$ sec^{-1})
0.825	26.780	1.623	6.540
0.850	24.580	1.503	3.546
0.875	22.700	1.397	1.983
0.900	21.090	1.303	1.141
0.925	14.830	0.210	0.366
0.950	10.910	0.140	0.146
0.975	6.505	0.070	0.036
1.000	0.000	0.000	0.000

Table 6d. Variation of densification rate by individual mechanisms with relative density at 900°C and 105 MPa

Relative density	Boundary diffusion ($\times 10^4$ sec^{-1})	Nabarro-Herring and Coble creep ($\times 10^4$ sec^{-1})	Power-law creep ($\times 10^4$ sec^{-1})
0.925	22.240	0.314	2.778
0.950	16.360	0.210	1.105
0.975	9.757	0.105	0.273
1.000	0.000	0.000	0.000

An important observation is that at a pressure of 17.5 MPa, boundary diffusion is always the dominant mechanism within the temperature range studied. At low temperatures and pressures greater than 17.5 MPa, the dominant mechanism changed from power-law creep to boundary diffusion as the porosity decreased (density increased). However, increasing temperatures at a given pressure caused narrower relative density ranges where power-law creep dominated. At the highest hot-pressing temperature of 900°C, power-law creep did not dominate the densification process at any relative density.

Increasing pressures at any temperature first caused power-law creep to appear as the dominant mechanism (≈ 20 MPa) at low relative densities. Still increased pressure widened the range of relative densities where power-law creep was dominant. At all times, however, the final stage of densification (D > 90%) was dominated by boundary diffusion. Such behavior was most pronounced at low temperatures, i.e., 800°C, where the yield strength is high. This agrees well with the early predictions that increasing pressures, temperature, and time caused the dominant mechanism to change (Figures 3-6). The calculations also support the prediction that intergranular diffusion was responsible for the strengthening of grain boundaries and thus, the transgranular fracture observed on specimens prepared at 900°C and pressures higher than 17.5 MPa.

A more practical way of determining domains of dominance for each mechanism is to prepare densification maps. Figure 11 was prepared by employing the equations given in Table 1 and data presented in Table 3

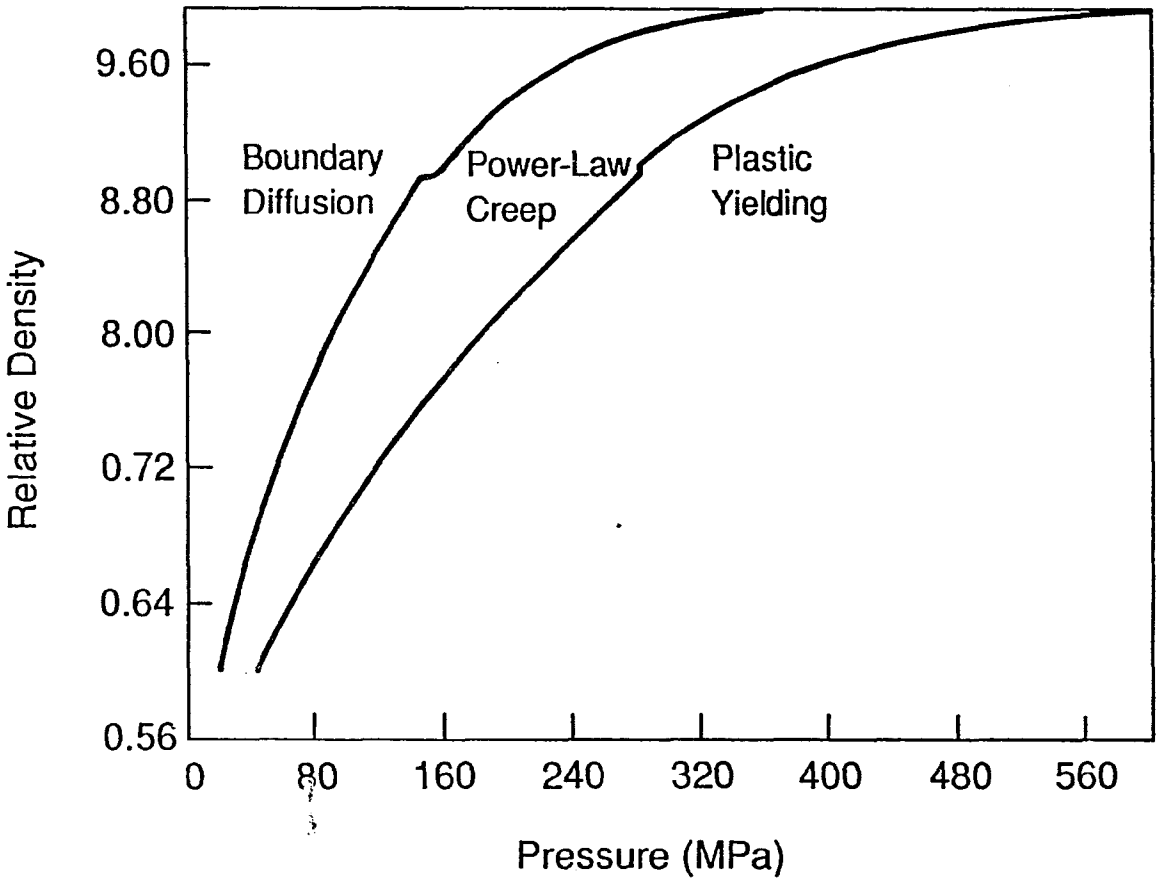

Figure 11. Densification map for hot pressing of ZnS at 800°C. Particle size = 0.35 μm, σ_y = 180 MPa, and ρ_o = 0.5

for T = 800°C. The boundary between plastic yielding and power-law creep was determined by calculating the densities reached by time independent plastic flow only. The borderline between boundary diffusion and power-law creep was determined by equating the rate expressions for these two mechanisms. Discontinuities at a relative density of 0.9 are the result of changing equations for initial and final stages of densification. The map shows that the hot-pressing conditions of P = 160 MPa and T = 800°C cause densification by power-law creep up to a relative density of about 0.91, but that achieving full density required boundary diffusion. The initial particle size distribution is, therefore, important in the hot-pressing of ZnS. As the temperature is increased, the densities that can be reached by plastic flow increase and the domain of power-law creep is narrowed.

Densities achieved experimentally in our laboratory in one minute for various pressures at 800°C are marked on Figure 11. It clearly shows that at a hot-pressing time of one minute, boundary diffusion has already become the dominant mechanism at all pressures at 800°C. Constant-time contours prepared for less than one minute are expected to cross borderline between power-law creep and boundary diffusion. Since we did not have any data at hot-pressing times less than one minute, however, we have not plotted these constant-time contours in Figure 11.

Note that the hot-pressing temperature was around 0.5 - 0.55 Tm, so that increasing temperature may be more effective than increasing

pressure to achieve full density. In agreement to this prediction, 99.9% dense specimens were prepared at 950°C and 105 MPa by hot-pressing for 18 minutes.

CONCLUSIONS

The present study of hot pressing has shown that it is possible to prepare ZnS compacts to very high relative densities with uniform, submicron grains. Starting powders with spherical, submicron particles are responsible for uniformity of the final microstructure and the lower pressure (<1/2 of that reported earlier) required to achieve near theoretical densities.

The dominant densification mechanism was determined using the experimental conditions employed and instantaneous relative density of the specimen. The initial stages of the densification obey the power-law creep model which quickly becomes less important with increasing density. Boundary diffusion dominates the final stage of densification.

REFERENCES CITED

1. H. J. McQueen and G. C. Kuczynski, J. Am. Ceram. Soc. 45 [7], 343 (1962).

2. Y. Fujita and T. Nitta, J. Am. Ceram. Soc. 65 [2], C18 (1982).

3. J. A. Savage, in Infrared Optical Materials and Their Antireflection Coatings (Adam Hilger Ltd., Bristol, England, 1985), p. 58.

4. J. A. Savage, K. L. Lewis, A. M. Pitt and R. H. L. Whitehouse, in SPIE, Vol. 505, Advances in Optical Materials, edited by S. Musikant (SPIE, Bellingham, WA, 1984).

5. J. A. Savage, in Infrared Optical Materials and Their Antireflection Coatings (Adam Hilger Ltd., Bristol, England, 1985), p. 100.

6. Eastman Kodak Company, British Patent #934421.

7. E. Carnall, Jr., J. Am. Ceram. Soc. 55 [11, 582 (1972).

8. A. S. Helle, K. E. Easterling, and M. F. Ashby, Acta Metall. 33 [12], [12], 2163 (1985).

9. M. F. Ashby, Acta Metall. 20, 887 (1972).

10. M. F. Ashby, Acta Metall. 29 [2], 259 (1981).

11. D. S. Wilkingson and M. F. Ashby, in Sintering and Catalysis, edited by G. C. Kuczynski (Plenum Press, New York, 1975).

12. M. R. Notis and R. M. Spriggs, in Sintering - New Developments, edited by M. M. Ristic (Elsevier, Amsterdam, 1979), p. 295).

13. M. R. Notis, R. H. Smoak and V. Krishnamachari, in Sintering and Catalysis, edited by G. C. Kuczynski (Plenum Press, New York, 1975), p. 493.

14. A. Celikkaya and M. Akinc, Submitted to J. Coll. Inter. Sci. (1988).

15. A. Celikkaya and M. Akinc, Submitted to J. Am. Ceram. Soc. (1988).

16. CRC Handbook of Chemistry and Physics, 67th Edition (CRC Press, Inc., Boca Raton, FL, 1987).

17. L. A. Xue and R. Raj, "Superplastic deformation of ZnS near its transformation temperature," Preprint, 1988.

18. H. Gobrecht, H. Nelkowski, J. W. Baars and M. Weight, Solid State Commun. 5, 777 (1967).

19. D. Laister and G. M. Jenkins, J. Mater. Sci. 8, 1218 (1973).

20. R. L. Stocker and M. F. Ashby, Scripta Metall. 7, 115 (1973).

ACKNOWLEDGMENTS

This work was supported in part by the Office of Naval Research and by Iowa State University. The authors are grateful to Professor M. F. Berard for critical review and Ms. Lynne Gaskill for typing the manuscript.

GENERAL CONCLUSIONS

Preparation, characterization and hot pressing of ZnS powders with monodispersed, spherical submicron particles was investigated. Kinetic expressions relating the rate of sulfide ion generation to temperature, pH and initial concentration of thioacetamide were derived. The initial zinc ion concentration was kept constant at 0.05 M at all times; higher concentrations caused agglomeration.

The particle morphology and type of particle size distribution depended critically on both the sulfide ion generation rate (at constant initial zinc ion concentration) and the chemical nature of supporting anions present in the system. In the presence of nitrate ions, which do not form strong complexes with zinc ion, the type of particle size distribution changed from monosize to bimodal and eventually, to a continuous distribution with increasing rates of sulfide ion generation. The mean particle diameter remained less than 1 μm in each case. Strong complex forming anions such as sulfate ions, on the other hand, caused monosized particles with a mean particle diameter of 3 μm with a unique fibrous structure at low rates of sulfide ion generation. The increasing sulfide ion generation rate caused a highly agglomerated, continuous particle size distribution preserving fibrous features. However, acetate ions, also being a strong complex former, resulted in monosized spherical particles of about 0.2 μm in all cases. The mean particle size decreased slightly with increasing sulfide ion generation rate. Intermediate rates of sulfide ion generation produced monosized particles of 0.5 μm in diameter in the

presence of chloride ions. At higher or lower rates of sulfide ion generation, particles similar to those obtained in the presence of sulfate ions were observed.

X-ray diffraction studies revealed only the β-ZnS (sphalerite) phase, except when the sulfide ion generation rate was low and sulfate ions were present in the system. A mixture of α-ZnS and β-ZnS was formed in such cases. Individual particles were determined to be polycrystalline with crystallite sizes of about 15 nm, only slightly larger than the critical nucleus size estimated from the Kelvin equation. Growth of particles occurred by diffusion-controlled aggregation of crystallites.

Hot-pressing experiments were conducted on ZnS powders prepared in the presence of nitrate ions having monosized particles of 0.35 μm in diameter. Compacts with near theoretical densities and uniform, submicron grains were prepared at hot pressing pressures half as high as those reported earlier at comparable temperatures and hot pressing times. Dominant densification mechanisms were power-low creep in the initial stages (relative densities around 0.6-0.7) and boundary diffusion in intermediate and final stages.

Samples having theoretical density with submicron grains were prepared at 950°C and 105 MPa in 18 minutes. The specimens were translucent to visible light. Modification of the hot pressing atmosphere is necessary for the future research.

LITERATURE CITED

1. P. Clasek, Texas Instruments, Inc., Office of Naval Research Meeting, China Lake, CA, Private communication, 1988.

2. I. W. Donald and P. W. McMillan, J. Mater. Sci. 13, 1151 (1978).

3. M. Akinc, Proposal submitted to Office of Naval Research, Arlington, VA, 1986.

ACKNOWLEDGMENTS

I would like to express my deepest appreciation to my major professor (and friend), Dr. Mufit Akinc, for his unceasing guidance and motivation during the past four years. I have gained much from his professional expertise.

I also would like to extend my thanks to Ms. Lynne Gaskill and Ms. Barb Dubberke for helping me with my endless last-minute requests.

Finally, Ms. Barb Dubberke is responsible for the expert typing of this thesis.